arXiv:2305.16189v3 [cs.LG] 20 Feb 2024

Martian time-series unraveled: A multi-scale nested approach with factorial variational autoencoders

Ali Siahkoohi[1*], Rudy Morel[2], Randall Balestriero[3], Erwan Allys[4], Grégory Sainton[5,6], Taichi Kawamura[6], Maarten V. de Hoop[1]

[1]Computational Applied Mathematics and Operations Research, Rice University, Houston, TX, USA.
[2]Center for Computational Mathematics, Flatiron Institute, New York, NY, USA.
[3]Independent Researcher, New York, NY, USA.
[4]Laboratoire de Physique, École Normale Supérieure, Paris, France.
[5]LERMA, Observatoire de Paris, PSL research Université, CNRS, Sorbonne Université, 75104, Paris, France.
[6]Université Paris Cité, Institut de physique du globe de Paris, CNRS, Paris, France.

*Corresponding author(s). E-mail(s): alisk@rice.edu;

Abstract

Unsupervised source separation involves unraveling an unknown set of source signals recorded through a mixing operator, with limited prior knowledge about the sources, and only access to a dataset of signal mixtures. This problem is inherently ill-posed and is further challenged by the variety of timescales exhibited by sources in time series data from planetary space missions. As such, a systematic multi-scale unsupervised approach is needed to identify and separate sources at different timescales. Existing methods typically rely on a preselected window size that determines their operating timescale, limiting their capacity to handle multi-scale sources. To address this issue, instead of directly operating in the time domain, we propose an unsupervised multi-scale clustering and source separation framework by leveraging wavelet scattering spectra that provide a low-dimensional representation of stochastic processes, capable of effectively distinguishing between different non-Gaussian stochastic processes. Nested within this representation space, we develop a factorial Gaussian-mixture variational autoencoder that is

trained to (1) probabilistically cluster sources at different timescales and (2) independently sample scattering spectra representations associated with each cluster. As the final stage, using samples from each cluster as prior information, we formulate source separation as an optimization problem in the wavelet scattering spectra representation space, aiming to separate sources in the time domain. When applied to the entire seismic dataset recorded during the NASA InSight mission on Mars, containing sources varying greatly in timescale, our multi-scale nested approach proves to be a powerful tool for disentangling such different sources, e.g., minute-long transient one-sided pulses (known as "glitches") and structured ambient noises resulting from atmospheric activities that typically last for tens of minutes. These results provide an opportunity to conduct further investigations into the isolated sources related to atmospheric-surface interactions, thermal relaxations, and other complex phenomena.

Keywords: source separation, unsupervised learning, clustering, multi-scale, time-series, variational autoencoders

1 Main

Source separation involves the often ill-posed problem of retrieving an *a priori* unknown number of source signals from an observed signal, often in the form of a time series. In order to tackle the ambiguity in retrieving the source signals, source separation methods incorporate available prior information about the sources—traditionally, by making assumptions about the regularity of the sources [1–6], e.g., sparsity or low-rank structure in some transform domain and certain distributional assumptions. While these traditional methods have been extensively studied and are well understood, their underlying regularity assumptions, if not realistic, can introduce bias into the outcome of the source separation process [5, 7]. For example, the eponymous classical independent component analysis (ICA) [8] source separation method and its variations, e.g., nonlinear ICA [9], generally impose assumptions such as non-Gaussianity and stationarity of sources, which makes their application extremely challenging in noisy environments and when dealing with data that we have very little prior knowledge, e.g., when dealing with data obtained from extraterrestrial missions. In fact, most real-world applications of ICA fall back to separating noise from signal [10, 11] as opposed to separate the sources within the signal that is embedded in noise.

In contrast to the conventional methods, data-driven source separation approaches are able to learn the prior information on sources (either implicitly or explicitly) from data. For example, supervised source separation methods [12–16] aim to separate sources by utilizing labeled training data, comprising pairs of sources and their mixtures. However, in domains with limited expert knowledge, obtaining labeled training data is often challenging, making supervised learning methods unsuitable. Furthermore, the use of synthetic data to artificially generate labels also proves challenging when the signal to be generated is not thoroughly understood. On the other hand, while unsupervised source separation methods can be applied in domains with no access to labeled data [17–22], they are not well-suited to handle source separation problems

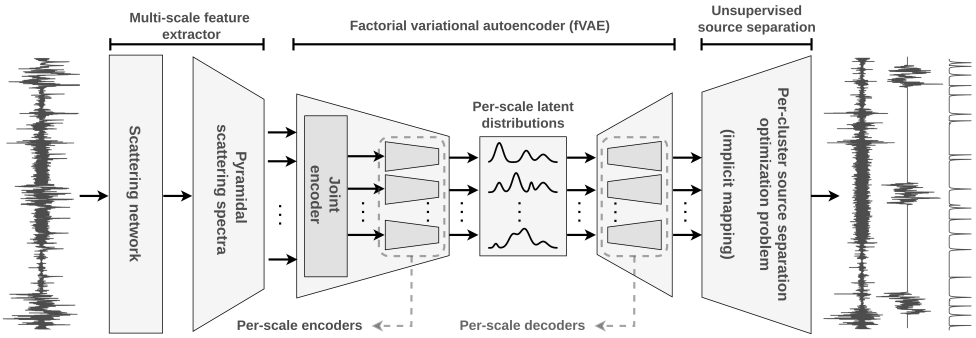

Fig. 1: A schematic diagram depicting the proposed unsupervised multi-scale clustering and source separation framework. In the factorial variational autoencoder schematic, multiple arrows going from one block to another indicate representations associated with different timescales.

where sources exhibit vastly varying timescales. This is partially due to their reliance on preselected window sizes that limits their usage to separating sources that span within the window's timescale. This limitation can be a critical obstacle in analyzing complex phenomena that involve sources with vastly different timescales.

To address this problem, we present an unsupervised multi-scale clustering and source separation framework that is capable of detecting and separating prominent sources in a dataset of signal mixtures. Our framework consists of the following building blocks (see Fig. 1 for a schematic diagram),

- **Pyramidal scattering spectra.** In light of the multi-scale nature of the sources, we develop our framework nested within the wavelet scattering spectra representation space [23]. This multi-scale representation of time series is based on the second moment of scattering network features [24] and is capable of capturing the non-Gaussian and multi-scale characteristics of stationary stochastic processes in the data. To take into account the existenc of multiple sources with varying timescales, we propose the pyramidal scattering spectra (first contribution), which involves averaging the wavelet scattering spectra representation at different timescales, resulting in a description of the data that captures non-Gaussian characteristics within different timescales;
- **Factorial variational autoencoder.** Within the pyramidal scattering spectra representation space, we introduce a factorial variant of Gaussian-mixture variational autoencoders [VAEs; 25–27] (second contribution), hereon referred to as fVAE, that simultaneously learns to probabilistically cluster sources at different timescales—the different factors—in the latent space and independently sample scattering spectra representations associated with each cluster. The former provides clusters of prominent sources in the dataset at different timescales, and the latter models the wavelet scattering spectra distribution of these sources, providing prior information necessary for source separation;

- **Unsupervised source separation.** We perform source separation by complementing the method proposed by Siahkoohi et al. [28] by the learned prior information regarding each source (third contribution). Our method for source separation involves solving an optimization problem over the unknown sources in the wavelet scattering spectra representations space. This is achieved by minimizing carefully selected and normalized loss functions that incorporate prior knowledge about the source of interest, ensure data-fidelity, and promote statistical independence between the recovered sources.

To demonstrate the applicability of our approach, we apply our approach to the full seismic dataset recorded by a seismometer on Mars during NASA's Interior Exploration using Seismic Investigations, Geodesy and Heat Transport (InSight) mission [29–31]. The InSight lander's seismometer—known as the SEIS instrument—detected marsquakes [32–35] and transient atmospheric signals, such as wind and temperature changes, that provide information about the Martian atmosphere [36] and enable studying the interior structure and composition of the Red Planet [37]. The signal recorded by the InSight seismometer is heavily influenced by atmospheric activity and surface temperature [38, 39]. These non-seismic signals largely vary in timescale from minutes to hours and it would be crucial to capture this in multiple timescale.

2 Results

Here, we offer a general overview of the proposed unsupervised multi-scale clustering and source separation framework necessary for communicating the results. A more in-depth presentation of the method, including details essential for reproducibility, is included in the Methods sections. As shown in Fig. 1, our framework consists of three main stages, described below.

In the initial stage, namely multi-scale feature extraction (indicated on the left in Fig. 1), we convert the data into the pyramidal scattering spectra representation space. The objective of this stage is to represent the data across significantly diverse timescales, ranging from less than a minute to an hour. This is particularly crucial when dealing with data that displays multi-scale structure, as adhering to a single window size would introduce bias to the analysis outcome. We present a systematic approach to extracting features from the data using a set of window sizes—rather than just one—by computing the scattering spectra over these window sizes. This is followed by an average pooling operation along the time, resulting in equally sized data representations at various timescales. This approach enables the joint execution of downstream tasks, such as clustering and source separation, over multiple timescales. We dive into the details of the pyramidal scattering spectra in the Methods section.

In the second stage, we train a generative model that learns a joint probabilistic description of these multi-scale representations (indicated in the middle of Fig. 1). The goal of this stage is to identify prominent sources in the dataset across several timescales, which will, in turn, be used as "prior information" in source separation (third stage, see below). To achieve this, we propose fVAEs where the scattering spectra representation of the data in each timescale is jointly mapped to a latent space, modeled via several Gaussian mixture models, each one associated with one timescale.

We derive a tractable evidence lower bound (ELBO) expression to jointly learn these Gaussian mixture models, ensuring the information in the pyramidal scattering spectra is preserved in the latent space. After training, the fVAE provides a probabilistic clustering of the data in various timescales while also serving as a prior in the downstream source separation stage.

In the final stage, we apply the technique proposed by Siahkoohi et al. [28] to separate the prominent source signals identified by the fVAE in the previous stage (shown on the right in Fig. 1). This approach involves solving an optimization problem in the scattering spectra space with the goal of separating a specific source of interest in the time domain, such as removing glitches or the wind imprint on seismic recordings. This method has the additional advantage of requiring minimal data snippets containing the source of interest to characterize the prior information needed for separation. By leveraging the fVAE, we can pinpoint these data snippets, and the optimization recovers a time-domain signal that explains the original time series in the scattering spectra space while closely aligning with the scattering spectra representation of the data snippets (samples from prior distribution).

2.1 Seismic records from the InSight mission

Martian seismic ambient signals consist of signals from various sources, each with different timescales. For instance, at shorter timescales, we expect to observe transient one-sided pulses known as glitches (tens of seconds in duration) [40]. These glitches likely stem from thermal cracks within the instruments' subsystems or atmospheric phenomena like dust devils—local low-pressure structures moving along the ambient wind (also lasting tens of seconds) [41]. Conversely, at longer timescales, we anticipate observing different phenomena such as regional winds whose direction and speed vary over time. These atmospheric phenomena strongly correlate with temperature, exhibiting a notable dependency on the local time at the station [41].

Moreover, the InSight SEIS instrument—a three-axis instruments (separated by 120°) called U, V, W—has recorded several major marsquakes, which hold significant importance for the insights they offer into the Martian subsurface [42]. However, due to their rarity in comparison to the aforementioned signal types (only 39 events over the course of four years [35]), clustering approaches are not naturally inclined to assign a cluster to marsquake recordings. Nevertheless, as we shall demonstrate, these signals tend to concentrate in the fVAE latent space associated with the correct timescale. This concentration serves as an indication of the rich structure of our multi-scale representation of this dataset.

2.2 Identification of clusters across different timescales

To obtain the aforementioned representation, we consider four different timescales to cover the range of timescales that the sources within the dataset of interest might exhibit. We utilize nine-component Gaussian mixture latent variables motivated by a previous study conducted by Barkaoui et al. [43], where the authors provided a single-scale clustering of this dataset using Gaussian mixture models. Since our approach will provide nine clusters per timescale, we expect some of the clusters to be redundant,

i.e., share a lot of similarities to one another. Based on existing studies on seismic data from the InSight mission [40, 41, 43], we selected the finest timescale to be 51.2 seconds, which is equivalent to a window size of 4^5 samples with 20 samples per second. This choice allows us to capture the diversity present in the one-sided pulses. To determine the subsequent timescales, we multiplied the previous timescale by a factor of four. While we do not expect to cluster broadband marsquakes [33] due to their infrequent occurrence compared to other sources, we set the largest window size to be 54.6 minutes, i.e., a window size of 4^8 samples. This window size covers marsquakes and other sources related to atmospheric-surface interactions [41].

While further investigation will be necessary to fully uncover the nature of the different clusters detected by our study, the results we obtained already demonstrate that the multi-scale approach successfully distinguishes the various phenomena observed in the Martian data. We provide information on all identified clusters within the four timescales considered in section A of the Appendix and present the notable clusters in this section. Specifically, Figs. 2 and 3 illustrate two noteworthy identified clusters for the finer (51.2 seconds and 3.4 minutes) and coarser (13.6 minutes and 54.6 minutes) timescales, respectively. To visualize clusters across the four timescales, we depict both the cluster occurrence time histogram along with ten aligned waveforms from that cluster. The cluster occurrence time histogram, i.e., the distribution of windows belonging to that cluster throughout the entire mission, will allow us to identify what times of the day a cluster may exhibit more occurrence, which in turn might reveal clusters that contain atmosphere-surface interaction signals. The aligned waveforms, on the other hand, are useful in identifying the main feature of each cluster. We adopt the approach outlined in [43] to generate the aligned waveforms. This procedure entails calculating, for each cluster within each timescale, the Pearson correlation coefficient between the most probable three component waveform assigned to that cluster (identified via the fVAE) and the remaining three components waveforms in that cluster, adjusted for lag to maximize correlation. Finally, we present the most probable waveform with each component plotted separately, along with nine other aligned waveforms (based on the lag producing the maximum correlation) for the waveforms exhibiting the highest correlation.

51.2-second timescale. At the finest timescale, we identified two clusters where the primary feature in both of the clusters are glitches (see Figs. 2a and 2b). The glitches in Fig. 2b contain a precursor, i.e., a high amplitude spike right before the glitch, and while not being restricted to a time interval during one Martian day, they tend to observed more frequently close to the sunset. This observation, albeit for glitches in general and not just glitches with precursors, has been independently made in prior work [43], which further confirm in nature of this cluster. Note that while the glitches in Fig. 2b uniformly contain one-sided pulses with increasing amplitude in the U components and decreasing amplitudes in the V and W components, this is due to visualizing aligned wavefoms and we do indeed detect other combinations in this cluster. Cluster 6 of this timescale (Fig. 2a), however, contains glitches without a precursor, has been detected in almost twice as many windows as cluster 7 (glitches with precursor, Fig. 2b), and has a significant peak around the sunset.

3.4-minute timescale. In the this timescale, the main feature of the clusters is often longer in timescale. For example, we obtain a distinct cluster that contains an oscillatory signal with an approximate 25-second period (see Fig. 2c). This cluster appears to mostly occur during Martian night, however, the oscillatory signal might also be present during the day but is drowned in high amounts of ambient daytime noise. No clear root cause for this oscillatory signal has yet been identified, but the analyses carried out show that there is no correlation with the pressure drops, but one has been noted with the wind. For the moment, any instrumental origin seems to have been ruled out. Note that at least two of the aligned waveforms in Fig. 2c also contain glitches, but a closer look reveals the existence of the oscillatory signal. In addition, we identify a cluster that contains one or more bursts of high-frequency, quickly dissipating energy (see Fig. 2d). It is worth noting that due to the high occurrence rate of glitches, the clusters identified in coarser times scales often also include glitches. However, except for the multi-glitch clusters, we argue glitches in coarser timescales are not the main characterizing feature of the clusters according to the aligned waveform plots.

13.6-minute timescale. While in this timescale we still obtain clusters dominated by glitches, we also see clusters associated with surface-atmosphere interactions to emerge. The noteworthy clusters are presented in Figs. 3a and 3b. The cluster in Fig. 3a clearly contains waveforms with a sharp onset and a following ringing oscillations. This feature is observed when a strong wind gust blows. Note that the length of this feature is longer than the high-frequency events with quickly dissipating energy in Fig. 2d. This might suggest that the winds captured in this cluster seem to be sustained longer. Interestingly, the cluster occurrence time histogram of this cluster in Fig. 2d suggests that these winds occur mostly before and after sunset. Another cluster that we observe in this timescale in shown in Fig. 3b. The waveforms associated with this cluster seem to have a distinct "noisy" pulse in the middle, with high-frequency, high-amplitude waveforms before and after it. These might suggest a cluster of dust devils. The occurence time histogram of this cluster also consistent with the time interval that dust devils are more frequently observed (09:00 to 15:00 LMST), which is confirmed by the InSight mission pressure sensors [44] as well as through the Pathfinder lander [45].

54.6-minute timescale. When focusing on the largest timescale, we again observe larger scale phenomena that were not captured in fine-scale clusters (recall Fig. 2). Notably, a wind cluster, as depicted in Fig. 3c, exhibits similar characteristic waveforms to the wind cluster in the 13.6-minute timescale (Fig. 3a), such as a sharp onset followed by ringing oscillations. However, upon examining the time histograms in Figs. 3a and 3c, it becomes evident that the cluster associated with Fig. 3a indicates a more significant dip after sunset compared to the other. Knowing that the wind speeds consistently decrease to very low levels approximately 2-4 hours after sunset [41], the significant dip in the time histogram of Fig. 3c can be due to the fact that there are fewer 54.6-minute long windows during this period that do not coincide with the low-wind interval compared to the number of 13.6-minute long windows. Finally, the cluster in Fig. 3d contains atmospheric signals related to the sunrise based on the cluster's occurrence time histogram and the gradual increase in waveform amplitude,

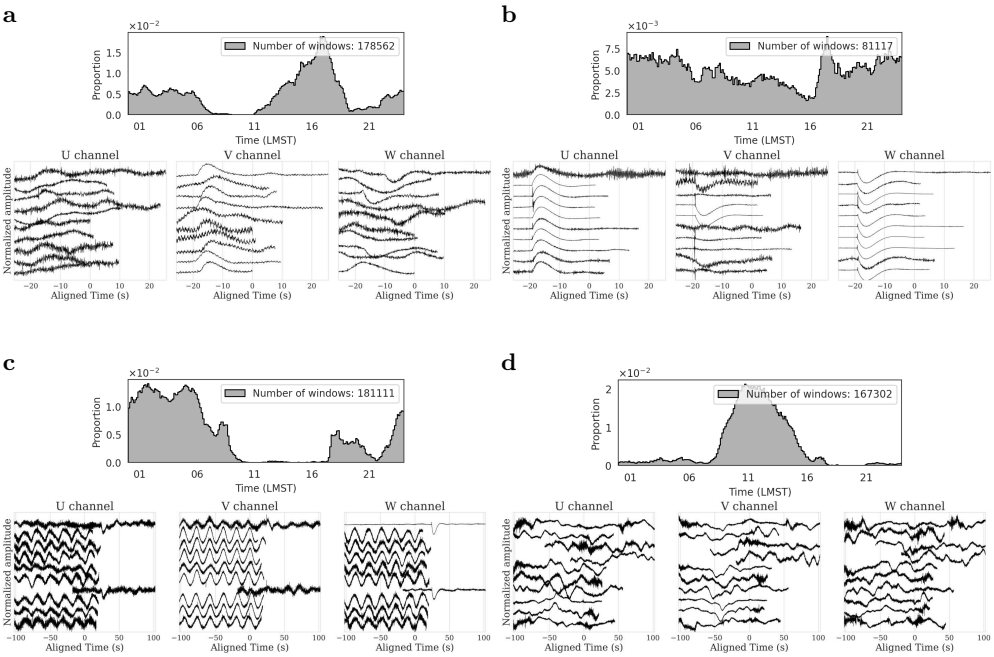

Fig. 2: The visualization of the cluster occurrence time histogram, obtained by aggregating data across the entire mission, and ten aligned waveforms of two clusters belonging to the finer timescales. **a**, cluster 6 at 51.2-second timescale. **b**, cluster 7 at 51.2-second timescale. **c**, cluster 6 at 3.4-minute timescale. **d**, cluster 8 at 3.4-minute timescale. The horizontal axis on the time histograms represents local mean solar time (LMST). The two clusters in Figs. 2a and 2b are associated with the 51.2-second timescale. Similarly, two clusters for the 3.4-minute timescale are shown in Figs. 2c and 2d. As expected, the finest time scale is capable of distinguishing between two types of glitches: with (Fig. 2a) and without (Fig. 2b) a precursor. According to their occurrence time histogram (horizontal axis on the time histograms is one Martian day), both of these glitch clusters have a tendency to appear more frequently around the Martian sunset. However, the glitch cluster without a precursor, seems to be more localized in time. In the 3.4-minute timescale, clusters are characterized by longer timescales. The cluster in Fig. 2c exhibits an oscillatory signal with an approximate 25-second period, predominantly occurring during Martian night and the cluster in Fig. 2d shows bursts of high-frequency, rapidly dissipating energy.

which is expected as the ambient noise recorded via the SEIS instrument during the day is consistently higher.

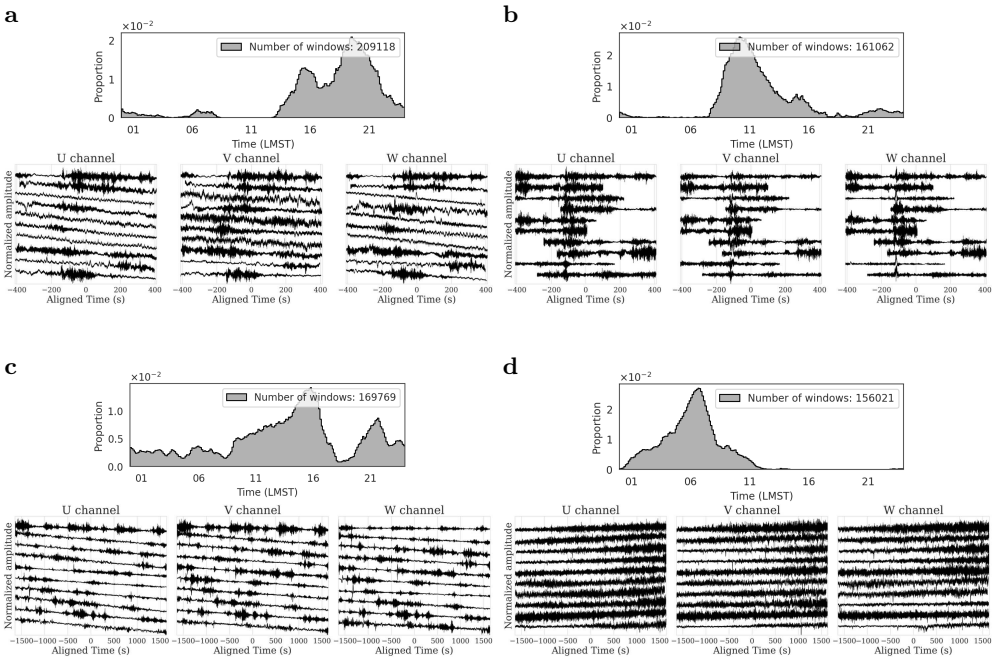

Fig. 3: The visualization of the cluster occurrence time histogram, obtained by aggregating data across the entire mission, and ten aligned waveforms of two clusters belonging to the coarser timescales. **a**, cluster 2 at 13.6-minute timescale. **b**, cluster 6 at 13.6-minute timescale. **c**, cluster 0 at 54.6-minute timescale. **d**, cluster 1 at 54.6-minute timescale. The horizontal axis on the time histograms represents local mean solar time (LMST). The two clusters in Figs. 3a and 3b are associated with the 13.6-minute timescale. Similarly, two clusters for the 54.6-minute timescale are shown in Figs. 3c and 3d. When focusing on coarser timescales, we start to see events that were not captured in the fine timescale clusters. Notably, Figs. 3a and 3c show some characteristic waveforms with a sharp onset and a following ringing oscillations. Such waveforms are observed when a strong wind gusts is blowing. This is also consistent with the occurrence time histogram of these clusters, which are localized in time [41]. Fig. 3d shows a cluster of waveform dominated by sunrise-related surface-atmospheric interactions. This can be inferred based on the cluster's occurrence time histogram as well as the gradual increase in waveform amplitude, which is related to the higher ambient seismic noise during the Martian daytime.

2.3 Seasonal impacts on surface-atmosphere interactions

To gain deeper insights into atmospheric-surface interactions, we investigate the impact of seasonal changes on the cluster occurrence time histograms. Using the clustered windows from all timescales, we computed occurrence time histograms for each cluster using aggregated data from all four seasons on Mars. We superimposed the per-season occurrence time histograms for all the clusters presented in Figs. 2 and 3,

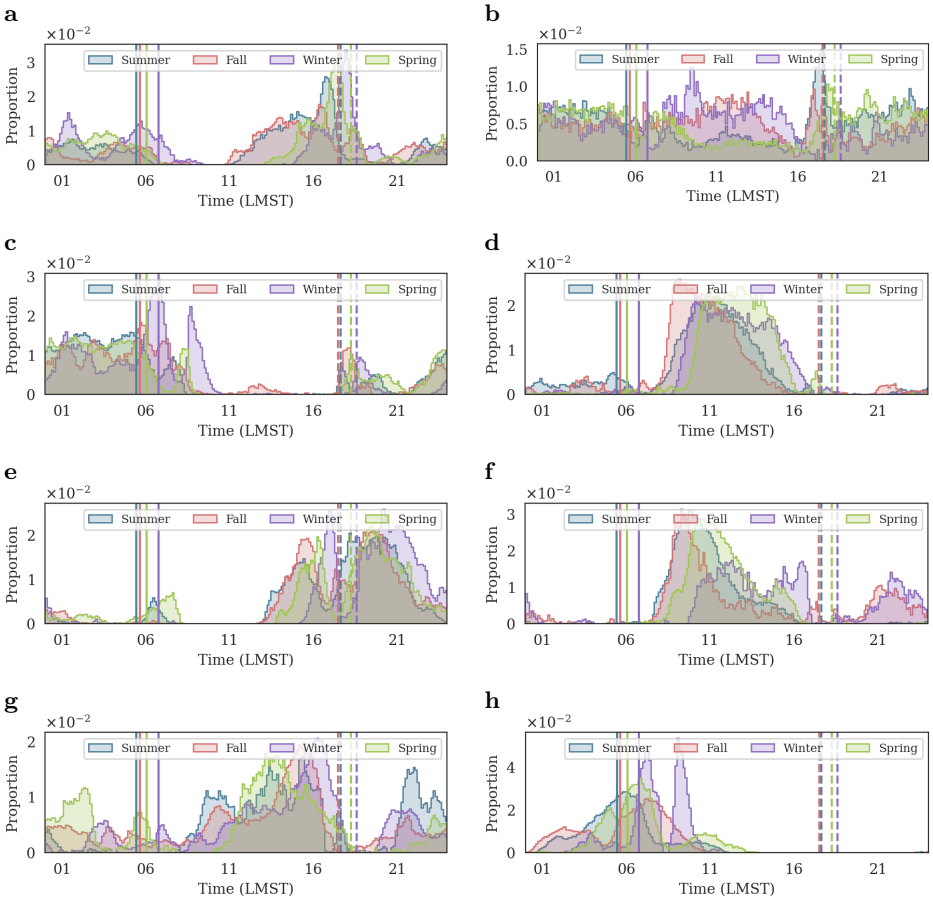

Fig. 4: An overlay of occurrence time histograms of selected clusters within four timescales where time histograms are obtained by aggregating data from Martian local spring (green), summer (blue), fall (red), and winter (purple). **a**, cluster 6 at 51.2-second timescale. **b**, cluster 7 at 51.2-second timescale. **c**, cluster 6 at 3.4-minute timescale. **d**, cluster 8 at 3.4-minute timescale. **e**, cluster 2 at 13.6-minute timescale. **f**, cluster 6 at 13.6-minute timescale. **g**, cluster 0 at 54.6-minute timescale. **h**, cluster 1 at 54.6-minute timescale. The horizontal axis on the time histograms represents local mean solar time (LMST). Each time histogram is associated with the clusters presented in Figs. 2 and 3 where each row represents a distinct timescale, with timescale increasing from top to bottom. The vertical and dashed lines correspond to average sunrise and sunset times over the associated season, respectively. Clusters with Martian daytime occurrences exhibited a tendency to shift in their peaks. Additionally, some clusters exhibit slight changes in their distribution, mainly involving a reduction or increase of their peaks as seasons change.

and overlay the per-season average sunrise (solid lines) and sunset (dashed lines) times to facilitate the interpretation of the histograms. Fig. 4 summarizes the results.

Upon visual inspection, we can confirm that the characteristic waveforms for all clusters at different time scales maintained the same structure as illustrated in Figs. 2 and 3. This ensures the nature of the clusters is unchanged across time, making comparing their histograms relevant. We make the following observations. While we acknowledge that not all variations observed in the time histograms can be solely attributed to seasonal changes (e.g., operational changes of the lander and having access to less data during the winter), we identified that clusters with Martian daytime occurrences exhibited a tendency to shift in their peaks. Furthermore, we also observe that some clusters exhibit slight changes in their distribution, mainly involving a reduction or increase of their peaks. Notable clusters involve the glitch clusters at the finest scale (see Figs. 4a and 4b). Specifically, we can observe that we have detected more waveforms during Martian daytime over the winter and fall seasons, which might be related to less ambient seismic noise due to lower temperatures, allowing our approach to identify more glitches during the day. In addition, as mentioned before, glitches tend to occur more near sunset, which we still can observe from the peak in per-season time histograms with the peak time clearly shifting with the average sunset time per season.

While we observe strong correlations between the occurrence time histograms and atmospheric conditions, it is worth mentioning that there are seismic signals in each cluster unaffected by seasonal changes. However, the heavy imprint of atmosphere-surface interactions skews the histograms nonetheless. In the next sections, we will indicate that indeed certain seismic events are concentrated in a few clusters, even though they are not the main characterizing feature of those clusters.

2.4 Unsupervised separation of prominent sources

Given access to clusters of glitches of wind-burst noises, in this section, we show that using samples from these clusters, we can perform source separation using the proposed approach in Siahkoohi et al. [28] (for details see the Methods section). In this approach, a particular source of interest can be separated from a given time series provided that we have access to several data snippets that does not contain that source of interest. Here explore separating glitches and the imprint of wind bursts. Figs. 5 and 6 summarizes the results, and we provide details and observations for each experiment below.

Glitch separation. For the glitch separation experiment, we select a 54.6-minute long waveform during Martian nighttime with several glitches (cf. Fig. 5a). We use 300 samples from cluster 5 in the 51.2-second timescale as its occurrence time histogram mostly concentrated during Martian night and its characteristic waveforms contain no glitches. Figs. 5b and 5c depicts the waveform after separation of glitches and the separated glitches, respectively. The last four rows of Fig. 5 illustrate the zoomed-in views of the results with columns from left to right being raw waveform, waveform after separation of glitches, and the separated glitch, respectively. These figures indicate the successful separation of glitches as the one-sided pulses are removed with minimal

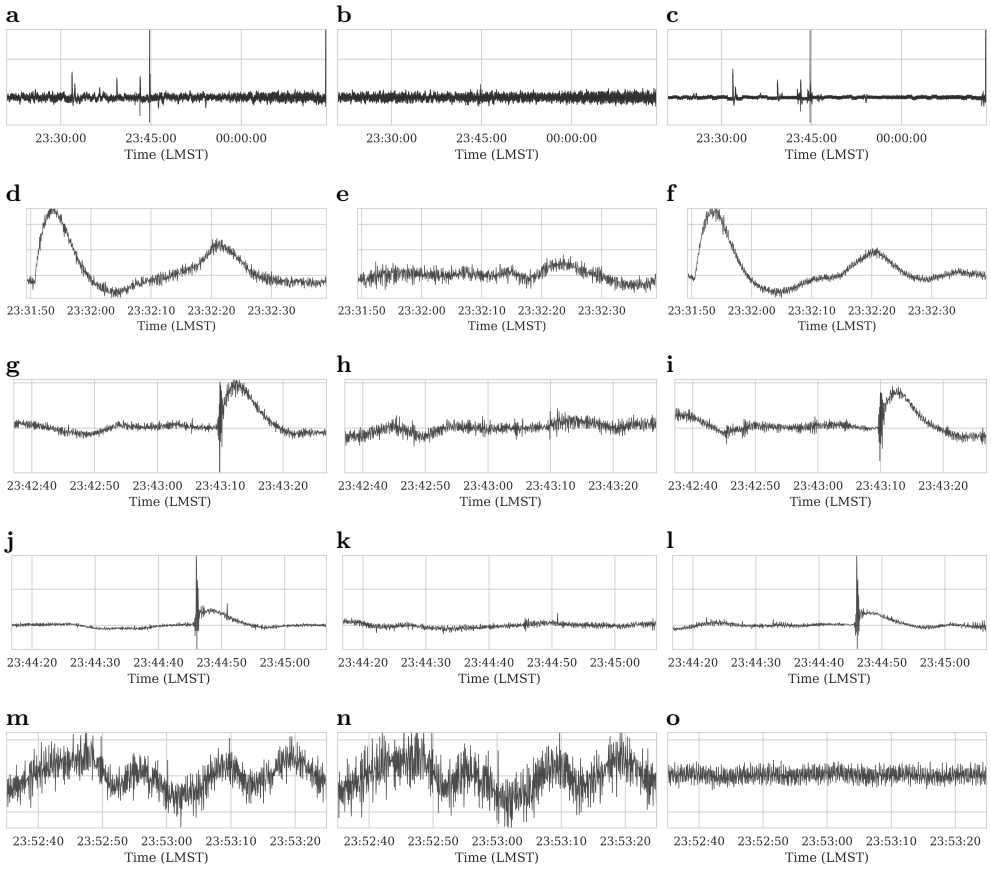

Fig. 5: Separating glitches from a waveform extracted from cluster 4 from the 54.6-minute timescale. **a**, raw waveform. **b**, waveform after separation. **c**, separated signal. **d**, **g**, **j**, **m**, raw waveform close-ups. **e**, **h**, **k**, **n**, waveform after separation close-ups. **f**, **i**, **l**, **o**, separated signal close-ups. The cluster that the raw waveform is selected from cluster is mostly concentrated during the Martian daytime and in order to remove glitches from this daytime waveform, we select as prior information 300 samples from cluster 5 in the 51.2-second timescale. This cluster has occurrence time histogram mostly concentrated during Martian night and its characteristic waveforms contain no glitches. As such, samples from this cluster would be good candidates for "backgrounds" signals that could allow for separating glitches.

changes to the rest of the waveform. Specifically, the last row of Fig. 5m indicates a zoomed-in view of a portion of the raw waveform that contains no glitches, and our method does not separate any coherent signal from the waveform (see the separated signal in Fig. 5o, which is a crucial property of our method.

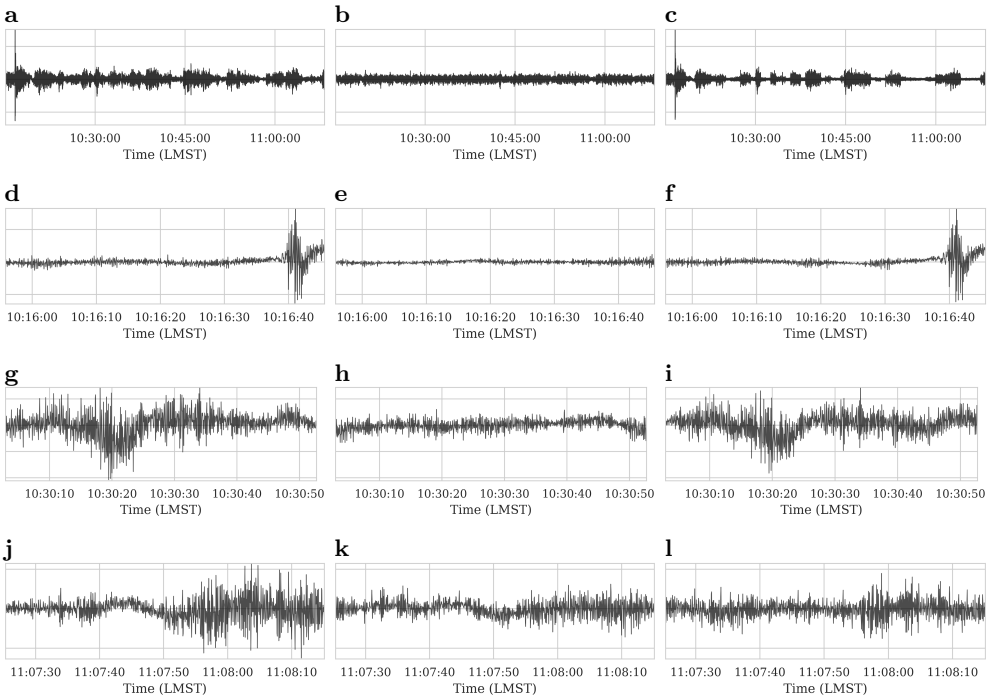

Fig. 6: Separating imprints of the wind from a waveform extracted from cluster 3 from the 54.6-minute timescale. **a**, raw waveform. **b**, waveform after separation. **c**, separated signal. **d**, **g**, **j**, raw waveform close-ups. **e**, **h**, **k**, waveform after separation close-ups. **f**, **i**, **l**, separated signal close-ups. The cluster that the raw waveform is selected from cluster is mostly concentrated during the Martian daytime and in order to remove glitches from this daytime waveform, we select as prior information 300 samples from clusters 1 and 6 in the 51.2-second timescale. These clusters have occurrence time histograms mostly concentrated during the day and their characteristic waveform exhibit no wind burst signatures. As such, samples from these clusters would be good candidates for "backgrounds" signals that could allow for separating wind burst related noises.

Wind burst imprint separation. For the wind burst imprint separation we select a Martian daytime 54.6-minute long waveform (cf. Fig. 6a). We use 300 samples from cluster 1 in the 51.2-second timescale as its occurrence time histogram mostly concentrated during Martian day and its characteristic waveforms contain no visible wind bursts. Figs. 6b and 6c depicts the waveform after separation of glitches and the separated glitches, respectively. The last four rows of Fig. 6 illustrate the zoomed-in views of the results with columns from left to right being raw waveform, waveform after separation of the wind burst imprint, and the separated wave burst imprint, respectively. These figures indicate the successful separation of wind burst imprints as the wind burst imprint (sharp onset followed by ringing oscillations) are removed with minimal changes to the rest of the waveform.

2.5 Latent space exploration of clusters

Towards better exploring the learned representation by fVAE, i.e., the per-scale representation obtained after the fVAE encoder, we visualize a low-dimensional representation of the entire dataset. We obtain this low-dimensional representation of the latent space via the UMAP algorithm [46], where we reduce the dimensionality of latent vectors from 32 (see the Methods section for a more detailed description of the architecture) to a two-dimensional representation. We obtain this two-dimensional representation independently for each scale and identify the most likely cluster that each point belongs to (computed through the fVAE) via colors. Fig. 7 contains these visualizations where each row corresponds to a different timescale with timescales increasing from top to bottom. To illustrate the importance of having a multi-scale representation, we overlay quality A and B broadband events (left column, with black star symbols) and the pressure drop events for each timescale (right column, with black circles). Note that due to our pyramidal scattering spectra construction mechanism, we have the same total number of latent samples in each scale while the number of samples identified as quality A and B events or pressure drops increases for larger timescales. Broadband events, i.e., marsquakes, typically have a length of 30–60 minutes and as such, even though we have observed very few of them during the mission and we cannot expect to have a cluster associated with them, we expect a good representation of data to concentrate them in the latent space. Similarly, we expect pressure drops, which have a timescale of less than a minute to be well concentrated in the smaller timescale representations.

We make the following observations. The clusters in 3.4-minute and 13.6-minute timescales (second and third rows of Fig. 7) compared to the finest and coarsest timescales have more clear boundaries, which suggest there are more structure in the data in these timescales. The 51.2-second timescale clusters are also relatively well separated, except for the area in the middle of Figs. 7a and 7b that contains mixed samples from several clusters. The 54.6-minute timescale cluster visualization, however, shows less cohesive structures and the points from several clusters are spread throughout the low-dimensional space. This might indicate that there are less effective number of clusters in this scale. Nonetheless, we importantly observe that the quality A and B broadband events are much more concentrated in the coarsest time scale (see Fig. 7g) compared to the others, with the concentration deteriorating as the timescale decreases. On the other hand, the pressure drops, which have a very short timescale, are very compactly situated in the finest timescale latent space while being spread across multiple clusters in the coarser timescales. These observations regarding the broadband and pressure drop events indicate that the learned representation in the fVAE indeed contains a lot of structure and is a multi-scale representation of data.

3 Discussion

In order to attain accurate source separation, having prior understanding of the sources is essential. Unsupervised source separation methods offer a solution when expert domain knowledge on the existing source signals is limited by learning to extract sources solely from a dataset of source mixtures. However, when dealing with data

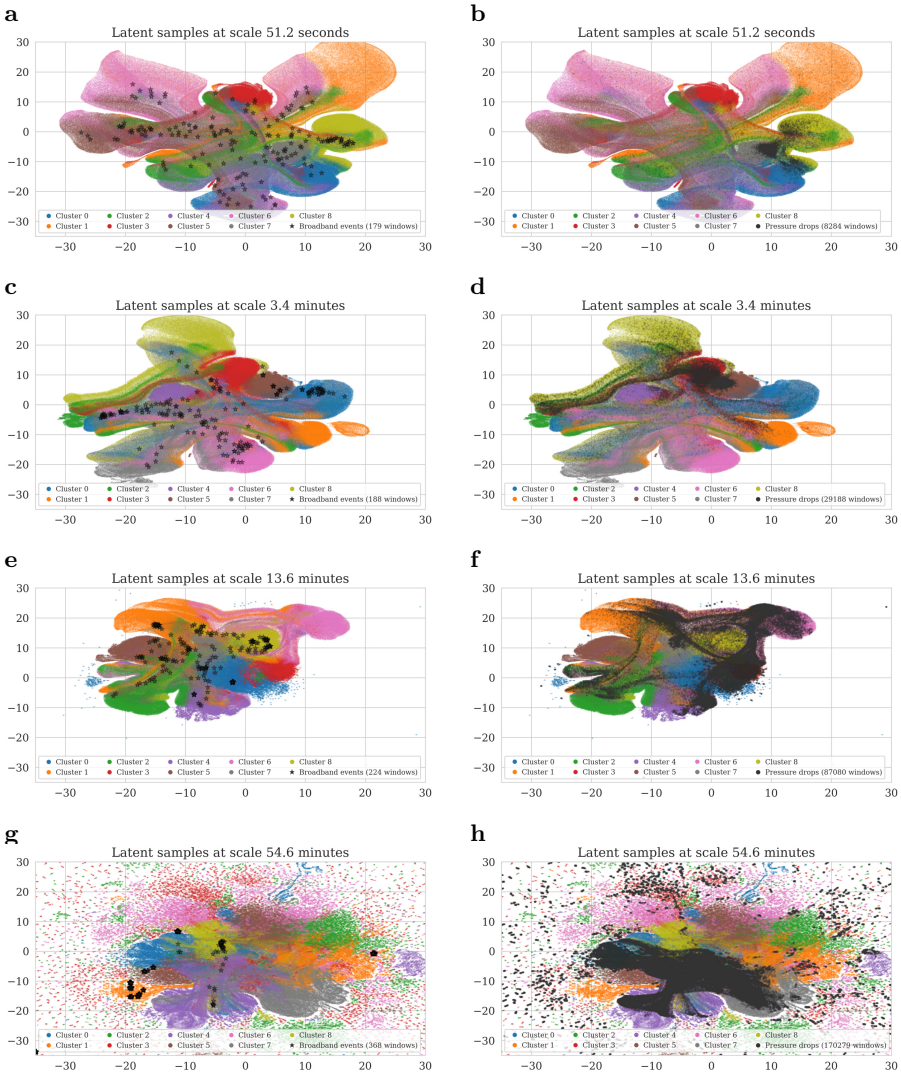

Fig. 7: fVAE latent space low-dimensional visualization, via UMAP [46], across four timescales overlaid with quality A and B broadband events or pressure drops. **a**, **b**, 51.2-second timescale. **c**, **d**, 3.4-minute timescale. **e**, **f**, 13.6-minute timescale. **g**, **h**, 54.6-minute timescale. The left column overlays quality A and B broadband events with star symbols, and the right column indicates pressure drops with black circles. Due to our pyramidal scattering spectra construction mechanism, we have the same total number of latent samples in each scale while the number of samples identified as quality A and B events or pressure drops increases for larger timescales. Nonetheless, we observe broadband events tend to concentrate better in the largest timescale, which corresponds to the timescale typically exhibited by marsquakes. Similarly, pressure drops that are very short in timescale concentrate very well in the shortest timescale.

containing sources of highly varied timescales, an architecture with appropriate inductive biases is needed to enable multi-scale treatment of source separation. In our work, we propose an approach using factorial variational autoencoders (fVAE) nested within the pyramidal wavelet scattering spectra representation. The intricate treatment of the multi-scale nature of the data—via pyramidal scattering spectra—can be also integrated in other clustering and source separation methods and its usage is not limited to the proposed fVAE architecture. Our results on data from NASA's InSight mission demonstrate that the multi-scale fVAE approach successfully identifies different non-seismic phenomena in the InSight data. While small timescale detect more the transient signal such as glitches, the large timescale captures more the global characteristics of the background noise, which is more likely related regional change in atmospheric conditions. The fVAE in turn enables unsupervised source separation by leveraging prior knowledge from the clusters. This approach makes minimal assumptions about the sources and provides a truly unsupervised method for source separation in non-stationary time-series with multi-scale sources.

Future work involves letting the mother wavelet in the scattering network to be learned, e.g., using [47]. In that setting, the mother wavelet is no longer specified a priori, but is rather parametrized by a few learnable parameters. Those parameters can then be learned to adapt the shape of the mother wavelet–and thus of all the signal statistics that the scattering network computes–to better minimize the loss at hand. Because the parametrization only adds a few parameters, overfitting is not an issue, even if noisy settings, as it was demonstrated in [48].

4 Methods

4.1 Pyramidal scattering spectra

Time-series data $\mathbf{x}$ recorded during space missions are typically non-stationary non-Gaussian noises. Such time-series are multi-scale in two respects. First, the signal $\mathbf{x}$ is a mixture of sources occurring at different time-scales, which contributes to its non-stationarity. Second, each individual source has variations on a wide range of scales, which can be observed by looking at a scalogram.

This section constructs a representation adapted to this doubly multi-scale nature of the data by building pyramidal wavelet scattering spectra. Such representation can be described as a multiple timescales average over diagonal correlation features on a two-layer convolutional neural network with predefined wavelet filters.

Wavelet scattering networks. A scattering network [24] is a cascade of wavelet operators $\mathbf{W}$ followed by nonlinear activation function (akin to a typical convolutional neural network). A wavelet transform $\mathbf{W}$ is a convolutional operator with predefined wavelet filters that extracts variations at separate scales. These filters include a low-pass filter $\varphi_J(t)$ and J complex-valued band-pass filters $\psi_j(t) = 2^{-j}\psi(2^{-j}t)$, $1 \leq j \leq J$, which are obtained by the dilation of a mother wavelet $\psi(t)$ that have zero-mean and a fast decay away from $t = 0$. The wavelet coefficient $\mathbf{W}\mathbf{x}(t, j) = x \star \psi_j(t)$ extracts variations of the input signal $\mathbf{x}(t)$ around time t at scale 2^j. In order to characterize time-evolution of the wavelet coefficients e.g., envelope modulation, we

apply a modulus $|\cdot|$ and cascade a second wavelet operator. The output of a two-layer scattering network S is $S(\mathbf{x}) := \left(\mathbf{W}\mathbf{x}\,,\,\mathbf{W}|\mathbf{W}\mathbf{x}|\right)^\top$, it extracts variations of signal $\mathbf{x}$ and its multi-scale envelopes $|\mathbf{W}\mathbf{x}|$ at different times and different scales. Even though these networks have been successfully employed in tasks such as intermittency analysis [49], clustering [48], event detection and segmentation [50] (with learnable wavelets), they are not sufficient to build an accurate description of a multi-scale process, as they fail to capture crucial dependencies across different scales [23].

Capturing non-Gaussian properties through scale dependencies. Sources $\mathbf{x}$ encountered in time-series studied in this paper can be considered are very often non-Gaussian processes. For sake of simplicity, let us assume $\mathbf{x}$ is a stationary source. If $\mathbf{x}$ were Gaussian then the different scale channels of a scattering networks would be independent, however it is not the case in practice and these dependencies were shown to be crucial to characterize the non-Gaussian stochastic structure of $\mathbf{x}$ [23]. Such dependencies can be captured by considering the correlation matrix $\mathbb{E}[S(\mathbf{x})S(\mathbf{x})^\top]$:

$$\mathbb{E}\begin{bmatrix} \mathbf{W}\mathbf{x}\,(\mathbf{W}\mathbf{x})^\top & \mathbf{W}\mathbf{x}\,(\mathbf{W}|\mathbf{W}\mathbf{x}|)^\top \\ \mathbf{W}|\mathbf{W}\mathbf{x}|\,(\mathbf{W}\mathbf{x})^\top & \mathbf{W}|\mathbf{W}\mathbf{x}|\,(\mathbf{W}|\mathbf{W}\mathbf{x}|)^\top \end{bmatrix}. \tag{1}$$

This matrix contains three types of coefficients. Correlation coefficients $\mathbb{E}[\mathbf{W}\mathbf{x}\,(\mathbf{W}\mathbf{x})^\top]$ come down to the wavelet power spectrum, which characterizes in particular the *roughness* of the signal. Correlation coefficients $\mathbb{E}[\mathbf{W}\mathbf{x}\,(\mathbf{W}|\mathbf{W}\mathbf{x}|)^\top]$ capture signed interaction between wavelet coefficients. In particular, they detect sign-asymmetry and time-asymmetry in $\mathbf{x}$ [23]. Finally, coefficients $\mathbb{E}\{\mathbf{W}|\mathbf{W}\mathbf{x}|\,(\mathbf{W}|\mathbf{W}\mathbf{x}|)^\top\}$ capture correlations between signal envelopes $|\mathbf{W}\mathbf{x}|$ at different scales. These correlations account for intermittency and envelope time-asymmetry [23].

Owing to the compression properties of wavelet operators [51] for the type of signals considered in this paper, these matrices are quasi-diagonal. We denote $\mathbb{E}[\mathrm{diag}\left(S(\mathbf{x})S(\mathbf{x})^\top\right)]$ an appropriate diagonal approximation of the full sparse matrix (1). The expectation $\mathbb{E}$ is replaced by a time average denoted by Ave (average pooling) whose size should be chosen as the typical duration of event $\mathbf{x}$. The wavelet scattering spectra representation is

$$\Psi(\mathbf{x}) := \mathrm{Ave}\left(S(\mathbf{x})\,,\,\mathrm{diag}\left(S(\mathbf{x})S(\mathbf{x})^\top\right)\right). \tag{2}$$

It extracts average and correlation features on a two-layer convolutional neural network with predefined wavelet filters. They are analogous to the features extracted in Gatys et al. [52] for generation. However, we do not train any weights in our representation. Owing to the compression properties of wavelet operators we obtain a low-dimensional representation. For a signal $\mathbf{x} \in \mathbb{R}^L$ of length L the scattering spectra contain approximately $\log_2^3(L)/6$ coefficients [23]. As a consequence, our representation, composed of order 1 and order 2 moments, can be estimated with low-variance which is be crucial for clustering and disentangling sources. One can also consider scattering cross-spectra between two signals $\mathbf{x}$ and $\mathbf{y}$, defined by $\Psi(\mathbf{x},\mathbf{y}) = \mathrm{Ave}\,\mathrm{diag}\left(S(\mathbf{x})S(\mathbf{y})^\top\right)$. They capture non-linear, non-Gaussian dependencies between signals $\mathbf{x},\mathbf{y}$.

Pyramidal averaging. Non-stationarity in the data $\mathbf{x}$ is in part explained by the presence of sources at different timescales. Our representation $\Psi(\mathbf{x})$ averages scattering spectra features on a certain window 2. If a source has a time-duration that is much smaller than the average window size, it will be averaged out, and the representation will contain little information about such a source. To take into account the variety of source timescales, we consider different averaging sizes in a causal manner. We replace Ave in (2) by a multi-scale average pooling operator $\text{Ave} = \big(\underset{t\in w_1}{\text{Ave}}\,, \ldots, \underset{t\in w_K}{\text{Ave}}\big)$. The windows $w_1 \subset \ldots \subset w_K$ have a pyramidal structure, they are of increasing size, all ending at the same time, $\underset{t\in w_1}{\text{Ave}}$ considers recent past while $\underset{t\in w_K}{\text{Ave}}$ considers distant past. To cover a large range of timescales with few factors we choose w_{k+1} to be four times longer than w_k. This defines a *pyramidal scattering spectra* representation $\Psi(x) = (\Psi_1(x), \ldots, \Psi_K(x))$ whose factor k is

$$\Psi_k(\mathbf{x}) := \underset{t\in w_k}{\text{Ave}}\,\big(S(\mathbf{x})\,,\,\text{diag}\,\big(S(\mathbf{x})S(\mathbf{x})^\top\big)\big). \tag{3}$$

The representation $\Psi(\mathbf{x})$ decomposes the variation in the stochastic structure of process $\mathbf{x}$ over time, through a multi-scale operator Ave.

4.2 Factorial Gaussian-mixture variational autoencoder (fVAE)

To efficiently perform source separation on our multi-scale representation, we require a generative model that can simultaneously cluster and sample. As Gaussian-mixture VAEs [25–27] are capable of learning highly structured, low-dimensional latent representations of data, they are a promising candidate for achieving our goals. The major open question remains on the structure of the mapping between the input space time-series and latent space cluster variables. As our aim is to cluster—or separate—sources co-occurring with different timescales, we propose a factorial variant to Gaussian-mixture VAEs to (1) jointly encode the wavelet scattering spectra representations of different timescales; (2) learn a low-dimensional Gaussian mixture latent variable for each timescale, enabling clustering; and (3) independently decode the latent representations of each timescale to be used as prior information in source separation. Note that independent decoding is crucial to ensure faithfulness of the per-source sampling process. In the next few subsections we describe our proposed generative model.

Generative model. Denote $\mathbf{u} := (\mathbf{u}_0, \ldots, \mathbf{u}_{s-1})$ the pyramidal wavelet scattering spectra random variable for s scales, which are our observed features of each signal. Our goal is to approximate the target joint distribution $p(\mathbf{u})$ through variational inference [VI; 53, 54] using samples of this distribution as training data. We achieve this by defining the following generative model,

$$p_\theta(\mathbf{u}, \mathbf{y}, \mathbf{z}) = p_\theta(\mathbf{u} \mid \mathbf{z}) p_\theta(\mathbf{z} \mid \mathbf{y}) p_\theta(\mathbf{y}) = \prod_{i=0}^{s-1} p_\theta(\mathbf{u}_i \mid \mathbf{z}_i)\, p_\theta(\mathbf{z}_i \mid y_i)\, p_\theta(y_i). \tag{4}$$

In this expression, $\mathbf{z}_i$ and y_i for $i = 0, \ldots, s-1$ represent the Gaussian mixture and Categorical latent variables for the i^{th} timescale, respectively. Furthermore, $\mathbf{z} :=$

$(\mathbf{z}_0, \ldots, \mathbf{z}_{s-1})$ and $\mathbf{y} := (y_0, \ldots, y_{s-1})$ represent the collection of latent variables for all timescales. We choose the following parametric distributions for these random variables,

$$\begin{aligned} p_\theta(y_i) &= \mathrm{Cat}\left(c_i^{-1}\mathbf{1}_{c_i}\right), \\ p_\theta(\mathbf{z}_i \mid y_i) &= \mathcal{N}\left(\mathbf{z}_i \mid \boldsymbol{\mu}_{z,i}(y;\boldsymbol{\theta}), \mathrm{diag}(\boldsymbol{\sigma}^2_{z,i}(y_i;\boldsymbol{\theta}))\right), \\ p_\theta(\mathbf{u}_i \mid \mathbf{z}_i) &= \mathcal{N}\left(\mathbf{u}_i \mid \boldsymbol{\mu}_{u,i}(\mathbf{z}_i;\boldsymbol{\theta}), \mathrm{diag}(\boldsymbol{\sigma}^2_{u,i}(\mathbf{z}_i;\boldsymbol{\theta}))\right), \quad i = 0, \ldots, s-1, \end{aligned} \tag{5}$$

where c_i represents the number of components in the Gaussian mixture latent distribution. $p_\theta(\mathbf{z}_i \mid y_i)$ is chosen as a Gaussian distribution with $\boldsymbol{\mu}_{z,i}(y;\boldsymbol{\theta})$ and $\boldsymbol{\sigma}_{z,i}(y_i;\boldsymbol{\theta})$ simply being learnable vectors for each $y_i \in \{0, \ldots, c_i - 1\}$, which amounts to a Gaussian mixture model for $\mathbf{z}_i$. Conditioned on $\mathbf{z}_i$, $\mathbf{u}_i$ is also defined to be a Gaussian distribution with mean $\boldsymbol{\mu}_{u,i}(\mathbf{z}_i;\boldsymbol{\theta})$ and diagonal covariance $\boldsymbol{\sigma}_{u,i}(\mathbf{z}_i;\boldsymbol{\theta})$ parameterized using deep nets. The generative model setup outlined above translates to having independent decoders—i.e., mappings from latent variables to scattering spectra representations—for each timescale. This approach facilitates the independent synthesis of scattering spectra representations for each timescale for the downstream source separation step. However, training this generative model necessitates the use of a latent posterior distribution inference model to enable tractable VI.

Inference model. The graphical model for the joint latent and data distribution (i.e., scattering spectra) described above necessitates marginalizing the Gaussian mixture and Categorical latent distributions to evaluate the likelihood of the parametric distribution $p_\theta(\mathbf{u})$. Unfortunately, this process is computationally infeasible due to the high-dimensionality of these distributions. To overcome this obstacle, we utilize amortized VI to approximate the latent posterior distribution $q(\mathbf{y}, \mathbf{z} \mid \mathbf{u})$. This amortized approximation uses the Evidence Lower Bound [ELBO; 25, 54] to approximate the model likelihood. To exploit the potential causal relationships between sources at different timescales we condition the latent posterior for each timescale on the wavelet scattering spectra representations for all timescales. This differs from the generative model that involved decoupled decoders for each timescale. To be precise, here is the factorization we employ for VI that enables clustering of the input data

$$q_\phi(\mathbf{z}, \mathbf{y} \mid \mathbf{u}) = q_\phi(\mathbf{z} \mid \mathbf{y}, \mathbf{u}) q_\phi(\mathbf{y} \mid \mathbf{u}) = \prod_{i=1}^{s} q_\phi(\mathbf{z}_i \mid y_i, \mathbf{u}) q_\phi(y_i \mid \mathbf{u}). \tag{6}$$

In the above expression, the pyramidal scattering spectra representation is used to infer the per-scale cluster, which in turn determines the per-scale, per-cluster Gaussian latent distribution (associated component in the Gaussian mixture model). We use the following parameterizations to learn an amortized latent posterior model:

$$\begin{aligned} q_\phi(y_i \mid \mathbf{u}) &= \mathrm{Cat}\left(\boldsymbol{\pi}_i(\mathbf{u};\boldsymbol{\phi})\right), \\ q_\phi(\mathbf{z}_i \mid y_i, \mathbf{u}) &= \mathcal{N}\left(\mathbf{z}_i \mid \boldsymbol{\mu}_{z,i}(\mathbf{u}, y_i;\boldsymbol{\phi}), \mathrm{diag}(\boldsymbol{\sigma}^2_{z,i}(\mathbf{u}, y_i;\boldsymbol{\phi}))\right), \quad i = 0, \ldots, s-1, \end{aligned} \tag{7}$$

where $\boldsymbol{\pi}_i(\mathbf{u};\boldsymbol{\phi})$, parameterized by a deep net, represents the cluster membership probabilities for pyramidal scattering spectra input $\mathbf{u}$ at the i^{th} timescale. Since the inferred latent variable encodes information regarding the cluster membership of $\mathbf{u}$, we explicitly provide both $\mathbf{u}$ and y_i to deep net parameterizations of its mean $\boldsymbol{\mu}_{z,i}(\mathbf{u}, y_i;\boldsymbol{\phi})$ and diagonal covariance $\boldsymbol{\sigma}^2_{z,i}(\mathbf{u}, y_i;\boldsymbol{\phi})$. With the generative and inference models defined, we derive the objective function for training the fVAE.

Training objective function. Training the fVAE involves minimizing the reverse Kullback-Leibler (KL) divergence between the parameterized and true joint distribution,

$$\mathbb{KL}\left(p(\mathbf{u}) \,||\, p_\theta(\mathbf{u})\right) = \mathop{\mathbb{E}}_{\mathbf{u}\sim p(\mathbf{u})}\Big[\underbrace{\log p(\mathbf{u})}_{\text{constant w.r.t. } \boldsymbol{\theta}} - \log p_\theta(\mathbf{u})\Big] = \mathop{\mathbb{E}}_{\mathbf{u}\sim p(\mathbf{u})}\Big[-\log p_\theta(\mathbf{u})\Big] + \text{const.} \tag{8}$$

As mentioned earlier, computing the likelihood of the graphical model is intractable due to required marginalization over $\mathbf{y}$ and $\mathbf{z}$ in equation (4). As a result, we approximate the likelihood with ELBO, which amounts to computing the expectation of joint distribution in equation (4) with respect to the latent posterior distribution, leading to the following training optimization problem:

$$\begin{aligned}
&\min_{\boldsymbol{\theta}} \mathop{\mathbb{E}}_{\mathbf{u}\sim p(\mathbf{u})}\Big[-\log p_\theta(\mathbf{u})\Big] \le \min_{\boldsymbol{\theta},\boldsymbol{\phi}} \mathop{\mathbb{E}}_{\mathbf{u}\sim p(\mathbf{u})} \mathop{\mathbb{E}}_{\mathbf{z},\mathbf{y}\sim q_\phi(\mathbf{z},\mathbf{y}|\mathbf{u})}\Big[-\log \frac{p_\theta(\mathbf{u},\mathbf{y},\mathbf{z})}{q_\phi(\mathbf{z},\mathbf{y}\mid\mathbf{u})}\Big] \\
&= \min_{\boldsymbol{\theta},\boldsymbol{\phi}} \sum_{i=1}^{s} \mathop{\mathbb{E}}_{\mathbf{u}\sim p(\mathbf{u})}\Big[\mathop{\mathbb{E}}_{\mathbf{z}_i\sim q_\phi(\mathbf{z}_i|y_i,\mathbf{u})} \underbrace{\big[-\log p_\theta(\mathbf{u}_i\mid\mathbf{z}_i)\big]}_{\text{Per-scale reconstruction loss}} + \underbrace{\mathbb{KL}\left(q_\phi(y_i\mid\mathbf{u}) \,||\, p_\theta(y_i)\right)}_{\text{Categorical prior on } y_i} \\
&\qquad + \mathop{\mathbb{E}}_{y_i\sim q_\phi(y_i|\mathbf{u})} \underbrace{\big[\mathbb{KL}\left(q_\phi(\mathbf{z}_i\mid y_i,\mathbf{u}) \,||\, p_\theta(\mathbf{z}_i\mid y_i)\right)\big]}_{\text{Gaussian mixture prior on } \mathbf{z}_i}\Big].
\end{aligned} \tag{9}$$

The expectations in the optimization problem above can be approximated using Monte Carlo integration over samples from their respective distributions.

Architecture. The architecture of the fVAE primarily relies on fully connected layers. The input consists of concatenated pyramidal wavelet scattering spectra, which are then passed through the joint encoder. This module is composed of a series of fully connected residual blocks, totaling four blocks. Each block includes a fully connected layer that reduces the dimensionality of the concatenated features to a hidden dimension, here set to 1024. This is followed by a Batchnorm layer and LeakyReLU nonlinearity. The output of the residual block is then brought back to the input dimensionality using another fully connected layer, and the result is added to the input (skip connection) to form the output of the residual block. Thanks to the pyramidal scattering spectra representation, the joint encoder with skip connection preserves maximal information from each scale and learns to extract useful information for generative modeling and clustering of representations.

Moving on to the per-scale encoders, the output of the joint encoder is split among different scales, and each scale is fed to a per-scale encoder. These encoders consist of

compositions of four fully connected layers, Batchnorm, and LeakyReLU activations. The first layer changes the dimensionality of each scale's representation to the hidden dimension (1024), while the last layer reduces this hidden dimension to the latent dimension of 32. We parameterize the latent distribution of each scale as a Gaussian mixture model with nine components, where the mean and diagonal covariances are unknown vectors. On the decoding side, the per-scale decoders mirror the per-scale encoders and reconstruct the input multi-scale representation from the latent space.

Training details of the factorial variational autoencoder. We utilized the entire data recorded during the InSight mission [55] to train the fVAE. During training, we randomly reserved 10% of the data as validation data for tuning a set of hyperparameters. Following the approach of Barkaoui et al. [43], we employed nine clusters at each timescale. The fVAE was trained using the architecture outlined above, employing a hidden dimension of 1024 and a latent dimension of 32. The Adam optimization algorithm [56] was employed with a learning rate of 10^{-3}. Training was conducted for 1000 epochs, utilizing a batch size of 16384. To address non-differentiability concerns associated with the categiral distribution learning, we utilized the Gumbel-Softmax distribution, enabling a differentiable approximate sampling mechanism for categorical variables [27]. The initial temperature parameter for the Gumbel-Softmax distribution was set to 1.0, and we exponentially decayed the temperature to a minimum value of 0.5. Training takes approximately 51 hours on a Tesla V100. We repeated the training with multiple different random seeds and observed relatively good stability. Specifically, the main clusters are still present in different runs, albeit slight changes to the histogram exist (possibly due to the data points lying on the border of different mixture components).

4.3 Source separation for clusters identified by fVAE

In this section we aim to perform the source separation in the time domain, while the previous section was working in the scattering spectra space. We introduce an unsupervised source separation algorithm that is based on an optimization problem over the time domain with a loss function defined in the wavelet scattering spectra representation space. The pretrained fVAE provides a model for the distribution of sources in the scattering spectra space. We use this as prior information in our optimization problem. Combining these techniques allows for the identification and separation of unknown multi-scale sources within a given time window, aligning with the objectives of unsupervised source separation. This approach was initially introduced by Regaldo-Saint Blancard et al. [57], Delouis, J.-M. et al. [58] and recently adapted to single timescale unsupervised source separation by Siahkoohi et al. [28].

Denote $\mathbf{x}$ as a given time window that is the sum of unknown independent sources $\mathbf{s}_i,\ i = 1, \ldots, M$, possibly occurring at different timescales, with measurement noise $\boldsymbol{\nu}(t)$: $\mathbf{x}(t) = \sum_{i=1}^{M} \mathbf{s}_i(t) + \boldsymbol{\nu}(t) = \mathbf{s}_1(t) + \mathbf{n}(t)$ with $\mathbf{n}(t) = \boldsymbol{\nu}(t) + \sum_{i=2}^{N} \mathbf{s}_i(t)$. Our approach to source separation involves detecting the prominent sources in $\mathbf{x}(t)$ and separating them one-by-one. We assume that the source $\mathbf{s}_1(t)$ is associated to one of the clusters identified by our fVAE model and we wish to separate $\mathbf{s}_1$ from the mixture. To constrain this ill-posed problem, we incorporate prior knowledge in the form of

realizations $\{\mathbf{s}_1^i\}_{i=1}^N$, identified by the fVAE as samples from the same cluster as the unknown source. Using these samples, we define three loss terms that impose that the reconstructed source $\widetilde{\mathbf{s}}_1$ has the same statistics as the collected samples $\mathbf{s}_1^i$, as well as that $\mathbf{x} - \widetilde{\mathbf{s}}_1$ has the same statistics as $\mathbf{n}$. It also promotes statistical independence between $\mathbf{s}_1$ and $\mathbf{x} - \widetilde{\mathbf{s}}_1$. These loss terms are:

$$\begin{aligned}
\mathcal{L}_{\text{prior}}(\mathbf{s}_1) &= \sum_{i=1}^{N} \frac{\left\| \Psi_k(\mathbf{s}_1) - \Psi_k(\mathbf{s}_1^i) \right\|_2^2}{\sigma^2\big(\Psi_k(\mathbf{s}_1^i)\big)}, \\
\mathcal{L}_{\text{cross}}(\mathbf{s}_1) &= \sum_{i=1}^{N} \frac{\left\| \Psi_k\left(\mathbf{s}_1^i, \mathbf{x} - \mathbf{s}_1\right) \right\|_2^2}{\sigma^2\big(\Psi_k(\mathbf{s}_1^i, \mathbf{x})\big)}, \\
\mathcal{L}_{\text{data}}(\mathbf{s}_1) &= \sum_{i=1}^{N} \frac{\left\| \Psi_k\left(\mathbf{x} - \mathbf{s}_1 + \mathbf{s}_1^i\right) - \Psi_k\left(\mathbf{x}\right) \right\|_2^2}{\sigma^2\big(\Psi_k(\mathbf{x} + \mathbf{s}_1^i)\big)}.
\end{aligned} \tag{10}$$

The first loss term ensures consistency between the statistics of the recovered signal $\mathbf{s}_1$ with the statistics of the observed signals $\mathbf{s}_1^i$. The second loss term ensures that the reconstruction $\mathbf{x} - \mathbf{s}_1$ of $\mathbf{n}$ has implicitly the correct statistics by ensuring $\mathbf{n} + \mathbf{s}_1^i$ has consistent statistics with $\mathbf{x}$. Finally, the third loss term promotes statistical independence between the recovered source $\mathbf{s}_1$ and the recovered noise $\mathbf{n}$. To facilitate the optimization and to avoid having to choose weighting parameters, each loss term is normalized with respect to the standard deviation of each coefficient in Ψ_k. This way, $\sigma^2\left(\Psi_k(\mathbf{s}_1^i)\right)$ stands for the vector of variance of each coefficient in Ψ_k computed along different realizations $\mathbf{s}_1^i$, the same holds for $\sigma^2\left(\Psi_k(\mathbf{x} + \mathbf{s}_1^i)\right)$ and $\sigma^2\left(\Psi_k(\mathbf{s}_1^i, \mathbf{x})\right)$. Finally, we can now sum the normalized loss terms and define the reconstruction $\widetilde{\mathbf{s}}_1$ as the solution to the optimization problem

$$\widetilde{\mathbf{s}}_1 := \arg\min_{\mathbf{s}_1} \Big[\mathcal{L}_{\text{data}}(\mathbf{s}_1) + \mathcal{L}_{\text{prior}}(\mathbf{s}_1) + \mathcal{L}_{\text{cross}}(\mathbf{s}_1) \Big]. \tag{11}$$

The algorithm relies solely on constraints in the scattering spectra space, except for its initialization $\widetilde{\mathbf{s}}_1 = \mathbf{x}$, which contains precious information about the mixture of sources in the time domain.

References

[1] Cardoso, J.-F.: Source separation using higher order moments. In: International Conference on Acoustics, Speech, and Signal Processing, vol. 4, pp. 2109–2112 (1989). https://doi.org/10.1109/ICASSP.1989.266878

[2] Jutten, C., Herault, J.: Blind separation of sources, part I: An adaptive algorithm based on neuromimetic architecture. Signal Processing **24**(1), 1–10 (1991) https://doi.org/10.1016/0165-1684(91)90079-X

[3] Bingham, E., Hyvärinen, A.: A fast fixed-point algorithm for independent component analysis of complex valued ignals. International Journal of Neural Systems **10**(01), 1–8 (2000) https://doi.org/10.1142/S0129065700000028

[4] Nandi, A.K., Zarzoso, V.: Fourth-order cumulant based blind source separation. IEEE Signal Processing Letters **3**(12), 312–314 (1996) https://doi.org/10.1109/97.544786

[5] Cardoso, J.-F.: Blind signal separation: Statistical principles. Proceedings of the IEEE **86**(10), 2009–2025 (1998) https://doi.org/10.1109/5.720250

[6] Jutten, C., Babaie-Zadeh, M., Hosseini, S.: Three easy ways for separating nonlinear mixtures? Signal Processing **84**(2), 217–229 (2004) https://doi.org/10.1016/j.sigpro.2003.10.011

[7] Parra, L., Sajda, P.: Blind source separation via generalized eigenvalue decomposition. Journal of Machine Learning Research **4**, 1261–1269 (2003) https://doi.org/10.5555/945365.964305

[8] Lee, T.-W.: Independent Component Analysis: Theory and Applications. Springer, New York, NY (1998). https://doi.org/10.1007/978-1-4757-2851-4

[9] Hyvärinen, A., Pajunen, P.: Nonlinear independent component analysis: Existence and uniqueness results. Neural networks **12**(3), 429–439 (1999)

[10] Salimi-Khorshidi, G., Douaud, G., Beckmann, C.F., Glasser, M.F., Griffanti, L., Smith, S.M.: Automatic denoising of functional mri data: Combining independent component analysis and hierarchical fusion of classifiers. Neuroimage **90**, 449–468 (2014)

[11] Hoyer, P.: Independent component analysis in image denoising. Master's thesis, Helsinki University of Technology (1999)

[12] Jang, G.-J., Lee, T.-W.: A maximum likelihood approach to single-channel source separation. The Journal of Machine Learning Research **4**, 1365–1392 (2003)

[13] Hershey, J.R., Chen, Z., Le Roux, J., Watanabe, S.: Deep clustering: Discriminative embeddings for segmentation and separation. In: 2016 IEEE International Conference on Acoustics, Speech and Signal Processing, pp. 31–35 (2016). https://doi.org/10.1109/ICASSP.2016.7471631

[14] Ke, S., Hu, R., Wang, X., Wu, T., Li, G., Wang, Z.: Single channel multi-speaker speech separation based on quantized ratio mask and residual network. Multimedia Tools and Applications **79**(43), 32225–32241 (2020) https://doi.org/10.1007/s11042-020-09419-y

[15] Kameoka, H., Li, L., Inoue, S., Makino, S.: Supervised determined source separation with multichannel variational autoencoder. Neural Computation **31**(9), 1891–1914 (2019) https://doi.org/10.1162/neco_a_01217

[16] Wang, D., Chen, J.: Supervised speech separation based on deep learning: An overview. IEEE/ACM Transactions on Audio, Speech, and Language Processing **26**(10), 1702–1726 (2018)

[17] Févotte, C., Bertin, N., Durrieu, J.-L.: Nonnegative Matrix Factorization with the Itakura-Saito Divergence: With Application to Music Analysis. Neural Computation **21**(3), 793–830 (2009) https://doi.org/10.1162/neco.2008.04-08-771

[18] Drude, L., Hasenklever, D., Haeb-Umbach, R.: Unsupervised training of a deep clustering model for multichannel blind source separation. In: IEEE International Conference on Acoustics, Speech and Signal Processing, pp. 695–699 (2019)

[19] Wisdom, S., Tzinis, E., Erdogan, H., Weiss, R., Wilson, K., Hershey, J.: Unsupervised sound separation using mixture invariant training. In: Advances in Neural Information Processing Systems, vol. 33, pp. 3846–3857 (2020)

[20] Liu, S., Mallol-Ragolta, A., Parada-Cabaleiro, E., Qian, K., Jing, X., Kathan, A., Hu, B., Schuller, B.W.: Audio self-supervised learning: A survey. Patterns **3**(12), 100616 (2022) https://doi.org/10.1016/j.patter.2022.100616

[21] Denton, T., Wisdom, S., Hershey, J.R.: Improving bird classification with unsupervised sound separation. In: 2022 IEEE International Conference on Acoustics, Speech and Signal Processing, pp. 636–640 (2022). https://doi.org/10.1109/ICASSP43922.2022.9747202

[22] Neri, J., Badeau, R., Depalle, P.: Unsupervised blind source separation with variational auto-encoders. In: 29th European Signal Processing Conference, pp. 311–315 (2021). https://doi.org/10.23919/EUSIPCO54536.2021.9616154

[23] Morel, R., Rochette, G., Leonarduzzi, R., Bouchaud, J.-P., Mallat, S.: Scale Dependencies and Self-Similar Models with Wavelet Scattering Spectra (2022)

[24] Bruna, J., Mallat, S.: Invariant scattering convolution networks. IEEE Transactions on Pattern Analysis and Machine Intelligence **35**(8), 1872–1886 (2013) https://doi.org/10.1109/TPAMI.2012.230

[25] Kingma, D.P., Welling, M.: Auto-encoding variational Bayes. In: International Conference on Learning Representations (2014)

[26] N, S., Paige, B., Meent, J.-W., Desmaison, A., Goodman, N., Kohli, P., Wood, F., Torr, P.: Learning disentangled representations with semi-supervised deep generative models. In: Advances in Neural Information Processing Systems, vol. 30 (2017)

[27] Jang, E., Gu, S., Poole, B.: Categorical reparameterization with Gumbel-softmax. In: International Conference on Learning Representations (2017)

[28] Siahkoohi, A., Morel, R., de Hoop, M.V., Allys, E., Sainton, G., Kawamura, T.: Unearthing InSights into Mars: Unsupervised source separation with limited data. In: Proceedings of the 40th International Conference on Machine Learning, vol. 202, pp. 31754–31772 (2023)

[29] Giardini, D., Lognonné, P., Banerdt, W.B., Pike, W.T., Christensen, U., Ceylan, S., Clinton, J.F., Driel, M., Stähler, S.C., Böse, M., *et al.*: The seismicity of Mars. Nature Geoscience **13**(3), 205–212 (2020) https://doi.org/10.1038/s41561-020-0539-8

[30] Golombek, M., Warner, N., Grant, J., Hauber, E., Ansan, V., Weitz, C., Williams, N., Charalambous, C., Wilson, S., DeMott, A., *et al.*: Geology of the InSight landing site on Mars. Nature communications **11**(1), 1–11 (2020)

[31] Knapmeyer-Endrun, B., Kawamura, T.: NASA's InSight mission on Mars—first glimpses of the planet's interior from seismology. Nature Communications **11**(1), 1–4 (2020)

[32] Horleston, A.C., Clinton, J.F., Ceylan, S., Giardini, D., Charalambous, C., Irving, J.C.E., Lognonné, P., Stähler, S.C., Zenhäusern, G., Dahmen, N.L., Duran, C., Kawamura, T., Khan, A., Kim, D., Plasman, M., Euchner, F., Beghein, C., Beucler, E., Huang, Q., Knapmeyer, M., Knapmeyer-Endrun, B., Lekić, V., Li, J., Perrin, C., Schimmel, M., Schmerr, N.C., Stott, A.E., Stutzmann, E., Teanby, N.A., Xu, Z., Panning, M., Banerdt, W.B.: The far side of Mars: Two distant marsquakes detected by InSight. The Seismic Record **2**(2), 88–99 (2022) https://doi.org/10.1785/0320220007

[33] Ceylan, S., Clinton, J.F., Giardini, D., Stähler, S.C., Horleston, A., Kawamura, T., Böse, M., Charalambous, C., Dahmen, N.L., van Driel, M., Durán, C., Euchner, F., Khan, A., Kim, D., Plasman, M., Scholz, J.-R., Zenhäusern, G., Beucler, E., Garcia, R.F., Kedar, S., Knapmeyer, M., Lognonné, P., Panning, M.P., Perrin, C., Pike, W.T., Stott, A.E., Banerdt, W.B.: The marsquake catalogue from InSight, sols 0–1011. Physics of the Earth and Planetary Interiors **333**, 106943 (2022) https://doi.org/10.1016/j.pepi.2022.106943

[34] Panning, M.P., Banerdt, W.B., Beghein, C., Carrasco, S., Ceylan, S., Clinton, J.F., Davis, P., Drilleau, M., Giardini, D., Khan, A., Kim, D., Knapmeyer-Endrun, B., Li, J., Lognonné, P., Stähler, S.C., Zenhäusern, G.: Locating the largest event observed on Mars with multi-orbit surface waves. Geophysical Research Letters **50**(1), 2022–101270 (2023) https://doi.org/10.1029/2022GL101270

[35] InSight Marsquake Service: Mars Seismic Catalogue, InSight Mission; V14 2023-04-01. ETHZ, IPGP, JPL, ICL, Univ. Bristol (2023). https://doi.org/10.12686/a21

[36] Stott, A.E., Garcia, R.F., Chédozeau, A., Spiga, A., Murdoch, N., Pinot, B., Mimoun, D., Charalambous, C., Horleston, A., King, S.D., Kawamura, T., Dahmen, N., Barkaoui, S., Lognonné, P., Banerdt, W.B.: Machine learning and marsquakes: A tool to predict atmospheric-seismic noise for the NASA InSight mission. Geophysical Journal International **233**(2), 978–998 (2022) https://doi.org/10.1093/gji/ggac464

[37] Beghein, C., Li, J., Weidner, E., Maguire, R., Wookey, J., Lekić, V., Lognonné, P., Banerdt, W.: Crustal anisotropy in the Martian lowlands from surface waves. Geophysical Research Letters **49**(24), 2022–101508 (2022) https://doi.org/10.1029/2022GL101508

[38] Lognonné, P., Banerdt, W.B., Pike, W., Giardini, D., Christensen, U., Garcia, R.F., Kawamura, T., Kedar, S., Knapmeyer-Endrun, B., Margerin, L., *et al.*: Constraints on the shallow elastic and anelastic structure of mars from insight seismic data. Nature Geoscience **13**(3), 213–220 (2020)

[39] Lorenz, R.D., Spiga, A., Lognonné, P., Plasman, M., Newman, C.E., Charalambous, C.: The whirlwinds of Elysium: A catalog and meteorological characteristics of "dust devil" vortices observed by InSight on Mars. Icarus **355**, 114119 (2021) https://doi.org/10.1016/j.icarus.2020.114119

[40] Scholz, J.-R., Widmer-Schnidrig, R., Davis, P., Lognonné, P., Pinot, B., Garcia, R.F., Hurst, K., Pou, L., Nimmo, F., Barkaoui, S., Raucourt, S., Knapmeyer-Endrun, B., Knapmeyer, M., Orhand-Mainsant, G., Compaire, N., Cuvier, A., Beucler, E., Bonnin, M., Joshi, R., Sainton, G., Stutzmann, E., Schimmel, M., Horleston, A., Böse, M., Ceylan, S., Clinton, J., Driel, M., Kawamura, T., Khan, A., Stähler, S.C., Giardini, D., Charalambous, C., Stott, A.E., Pike, W.T., Christensen, U.R., Banerdt, W.B.: Detection, analysis, and removal of glitches from InSight's seismic data from Mars. Earth and Space Science **7**(11), 2020–001317 (2020) https://doi.org/10.1029/2020EA001317

[41] Banfield, D., Spiga, A., Newman, C., Forget, F., Lemmon, M., Lorenz, R., Murdoch, N., Viudez-Moreiras, D., Pla-Garcia, J., Garcia, R.F., Lognonné, P., Karatekin, Ö., Perrin, C., Martire, L., Teanby, N., Hove, B.V., Maki, J.N., Kenda, B., Mueller, N.T., Rodriguez, S., Kawamura, T., McClean, J.B., Stott, A.E., Charalambous, C., Millour, E., Johnson, C.L., Mittelholz, A., Määttänen, A., Lewis, S.R., Clinton, J., Stähler, S.C., Ceylan, S., Giardini, D., Warren, T., Pike, W.T., Daubar, I., Golombek, M., Rolland, L., Widmer-Schnidrig, R., Mimoun, D., Beucler, É., Jacob, A., Lucas, A., Baker, M., Ansan, V., Hurst, K., Mora-Sotomayor, L., Navarro, S., Torres, J., Lepinette, A., Molina, A., Marin-Jimenez, M., Gomez-Elvira, J., Peinado, V., Rodriguez-Manfredi, J.-A., Carcich, B.T., Sackett, S., Russell, C.T., Spohn, T., Smrekar, S.E., Banerdt, W.B.: The atmosphere of Mars as observed by InSight. Nature Geoscience **13**(3), 190–198 (2020) https://doi.org/10.1038/s41561-020-0534-0

[42] Stähler, S.C., Mittelholz, A., Perrin, C., Kawamura, T., Kim, D., Knapmeyer, M., Zenhäusern, G., Clinton, J., Giardini, D., Lognonné, P., Banerdt, W.B.: Tectonics of Cerberus Fossae unveiled by marsquakes. Nature Astronomy **6**(12), 1376–1386 (2022) https://doi.org/10.1038/s41550-022-01803-y

[43] Barkaoui, S., Lognonné, P., Kawamura, T., Stutzmann, É., Seydoux, L., Maarten, V., Balestriero, R., Scholz, J.-R., Sainton, G., Plasman, M., *et al.*: Anatomy of continuous Mars SEIS and pressure data from unsupervised learning. Bulletin of the Seismological Society of America **111**(6), 2964–2981 (2021)

[44] Chatain, A., Spiga, A., Banfield, D., Forget, F., Murdoch, N.: Seasonal variability of the daytime and nighttime atmospheric turbulence experienced by InSight on Mars. Geophysical Research Letters **48**(22), 2021–095453 (2021) https://doi.org/10.1029/2021GL095453

[45] Ferri, F., Smith, P.H., Lemmon, M., Rennó, N.O.: Dust devils as observed by Mars Pathfinder. Journal of Geophysical Research: Planets **108**(E12) (2003) https://doi.org/10.1029/2000JE001421

[46] McInnes, L., Healy, J., Saul, N., Großberger, L.: UMAP: Uniform manifold approximation and projection. Journal of Open Source Software **3**(29), 861 (2018) https://doi.org/10.21105/joss.00861

[47] Balestriero, R., Cosentino, R., Glotin, H., Baraniuk, R.: Spline filters for end-to-end deep learning. In: Proceedings of the 35th International Conference on Machine Learning, vol. 80, pp. 364–373 (2018)

[48] Seydoux, L., Balestriero, R., Poli, P., Hoop, M.d., Campillo, M., Baraniuk, R.: Clustering earthquake signals and background noises in continuous seismic data with unsupervised deep learning. Nature communications **11**(1), 3972 (2020) https://doi.org/10.1038/s41467-020-17841-x

[49] Bruna, J., Mallat, S., Bacry, E., Muzy, J.-F.: Intermittent process analysis with scattering moments. The Annals of Statistics **43**(1), 323–351 (2015) https://doi.org/10.1214/14-AOS1275

[50] Rodríguez, Á.B., Balestriero, R., De Angelis, S., Benítez, M.C., Zuccarello, L., Baraniuk, R., Ibáñez, J.M., Maarten, V.: Recurrent scattering network detects metastable behavior in polyphonic seismo-volcanic signals for volcano eruption forecasting. IEEE Transactions on Geoscience and Remote Sensing **60**, 1–23 (2021)

[51] Wornell, G.W.: Wavelet-based representations for the 1/f family of fractal processes. Proceedings of the IEEE **81**(10), 1428–1450 (1993) https://doi.org/10.1109/5.241506

[52] Gatys, L., Ecker, A.S., Bethge, M.: Texture synthesis using convolutional neural

networks. In: Advances in Neural Information Processing Systems, vol. 28 (2015)

[53] Jordan, M.I., Ghahramani, Z., Jaakkola, T.S., Saul, L.K.: An introduction to variational methods for graphical models. Machine Learning **37**(2), 183–233 (1999) https://doi.org/10.1023/A:1007665907178

[54] Blei, D.M., Kucukelbir, A., McAuliffe, J.D.: Variational inference: A review for statisticians. Journal of the American statistical Association **112**(518), 859–877 (2017)

[55] InSight Mars SEIS Data Service: SEIS raw data, Insight Mission. IPGP, JPL, CNES, ETHZ, ICL, MPS, ISAE-Supaero, LPG, MFSC (2019). 10.18715/SEIS.INSIGHT.XB_2016

[56] Kingma, D.P., Ba, J.: Adam: A method for stochastic optimization (2014)

[57] Regaldo-Saint Blancard, B., Allys, E., Boulanger, F., Levrier, F., Jeffrey, N.: A new approach for the statistical denoising of Planck interstellar dust polarization data. Astronomy & Astrophysics **649**, 18 (2021)

[58] Delouis, J.-M., Allys, E., Gauvrit, E., Boulanger, F.: Non-Gaussian modelling and statistical denoising of Planck dust polarisation full-sky maps using scattering transforms. Astronomy & Astrophysics **668**, 122 (2022) https://doi.org/10.1051/0004-6361/202244566

Appendix A Identified clusters and their representative waveforms

In this section, we present the complete set of nine clusters identified by the fVAE across four different time scales. Figs. A1, A3, A5 and A7 display the occurrence time histograms of these clusters for 51.2-second timescale, 3.4-minute timescale, 13.6-minute timescale, and 54.6-minute timescale, respectively, by aggregating data the entire mission. Additionally, we provide the representative aligned waveforms for each cluster at all time scales. Figs. A2, A4, A6 and A8 depict these waveforms for 51.2-second timescale, 3.4-minute timescale, 13.6-minute timescale, and 54.6-minute timescale, respectively.

Appendix B fVAE decoder reconstruction quality

In this section, we present the reconstructed input scattering spectra through the fVAE. Figs. B9 to B12 summarize the results for 51.2-second timescale, 3.4-minute timescale, 13.6-minute timescale, and 54.6-minute timescale, respectively. Each one of these figures show the input scattering spectra (in black) and the corresponding reconstructed input (in red) for the U, V, and W components of four randomly selected waveforms.

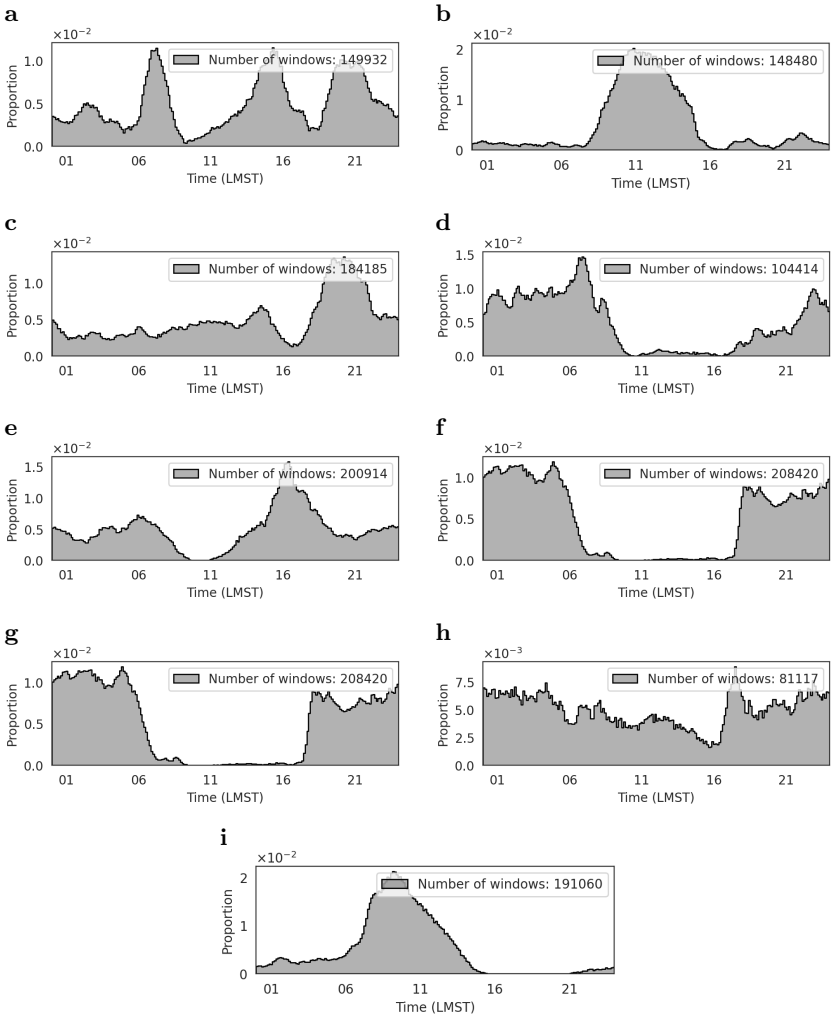

Fig. A1: The occurrence time histogram of all nine identified clusters within the 51.2-second timescale. The horizontal axis of the histograms represents the local mean solar time (LMST). Clusters 0–9 are shown in Figs. A1a to A1i, respectively.

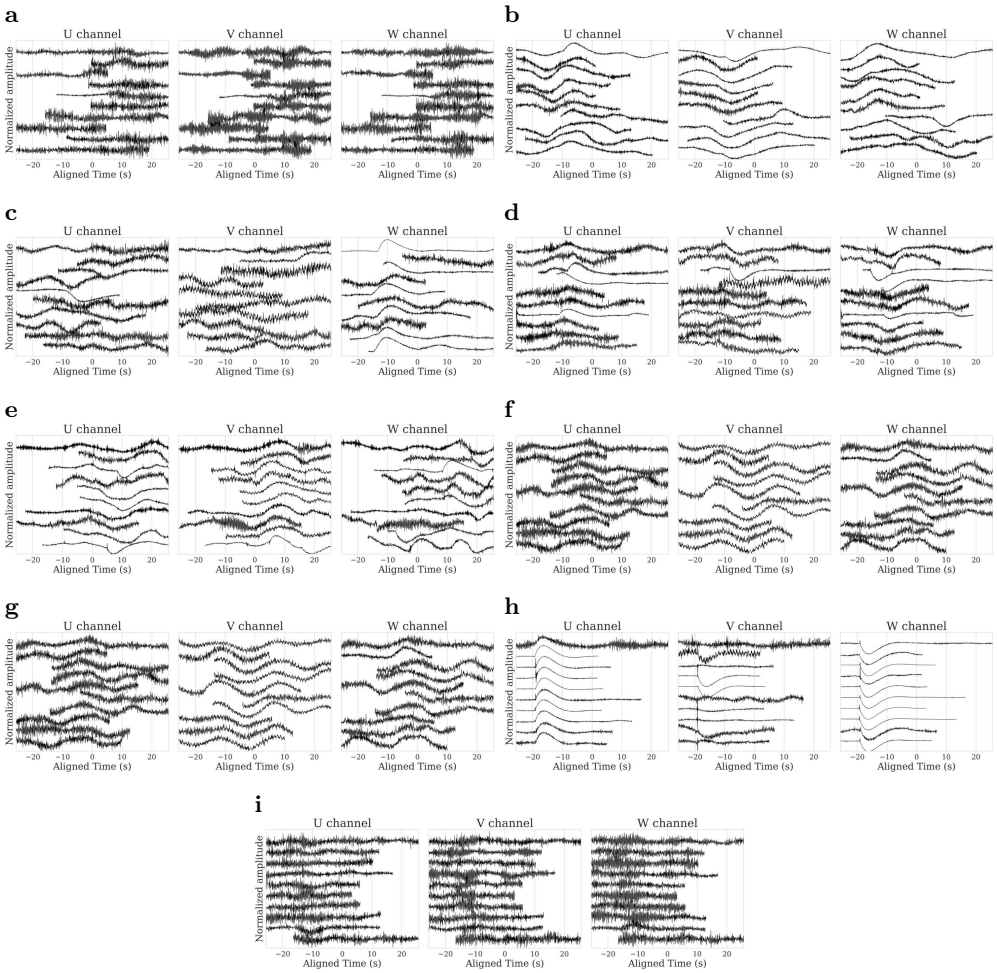

Fig. A2: The aligned waveforms of all nine identified clusters within the 51.2-second timescale. Clusters 0–9 are shown in Figs. A2a to A2i, respectively.

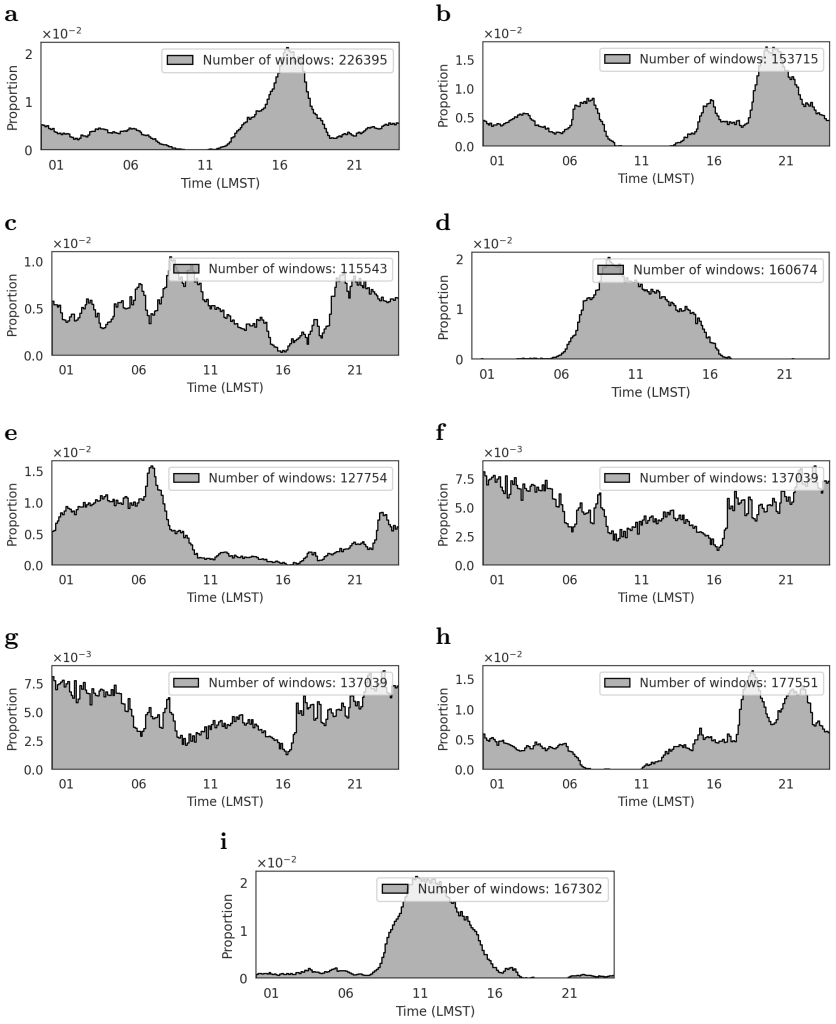

Fig. A3: The occurrence time histogram of all nine identified clusters within the 3.4-minute timescale. The horizontal axis of the histograms represents the local mean solar time (LMST). Clusters 0–9 are shown in Figs. A3a to A3i, respectively.

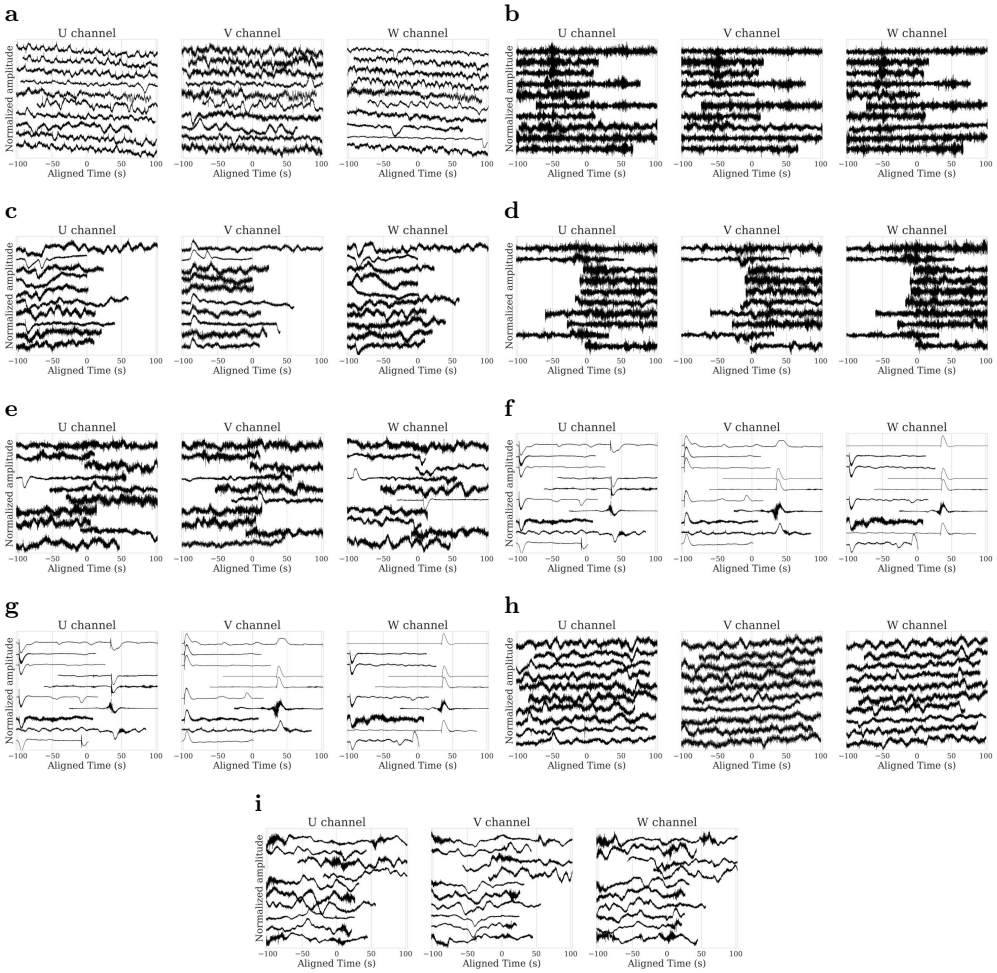

Fig. A4: The aligned waveforms of all nine identified clusters within the 3.4-minute timescale. Clusters 0–9 are shown in Figs. A4a to A4i, respectively.

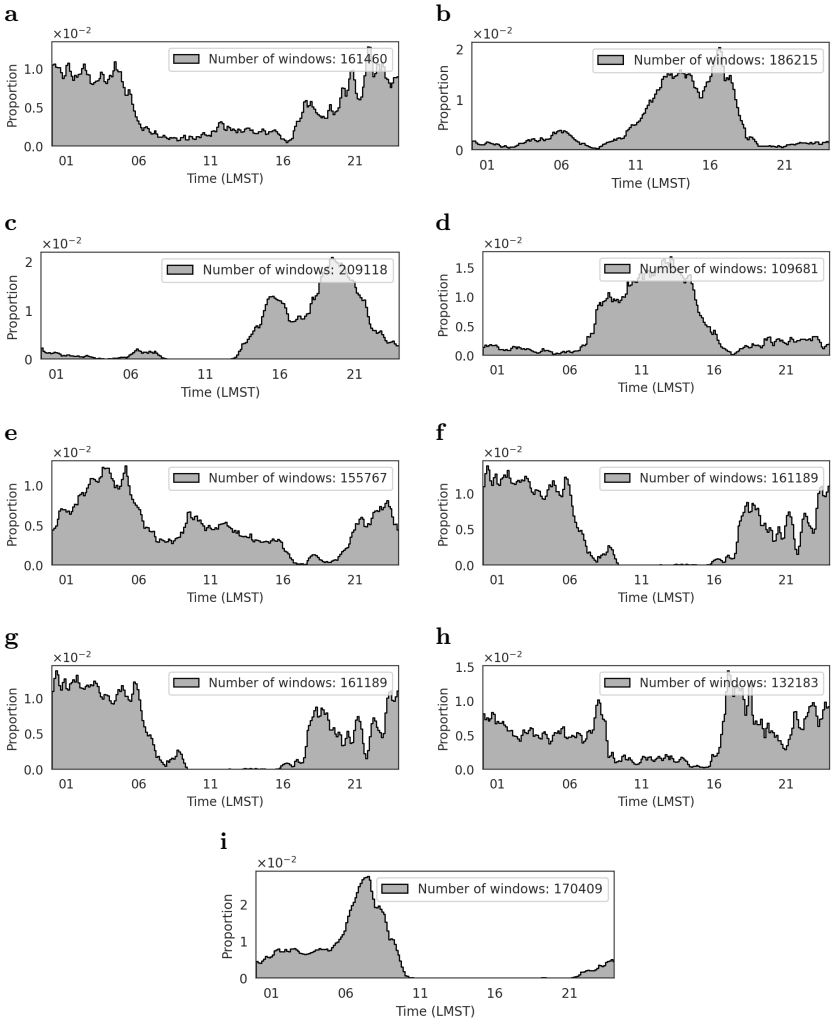

Fig. A5: The occurrence time histogram of all nine identified clusters within the 13.6-minute timescale. The horizontal axis of the histograms represents the local mean solar time (LMST). Clusters 0–9 are shown in Figs. A5a to A5i, respectively.

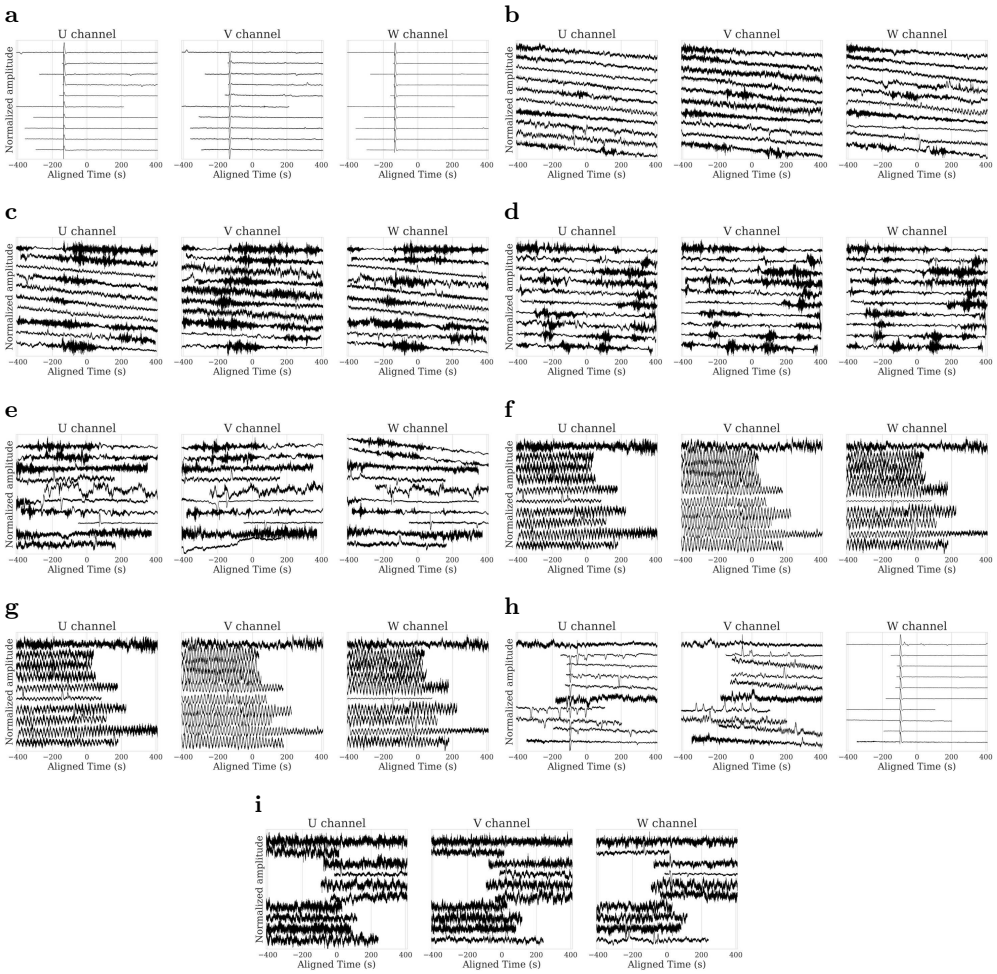

Fig. A6: The aligned waveforms of all nine identified clusters within the 13.6-minute timescale. Clusters 0–9 are shown in Figs. A6a to A6i, respectively.

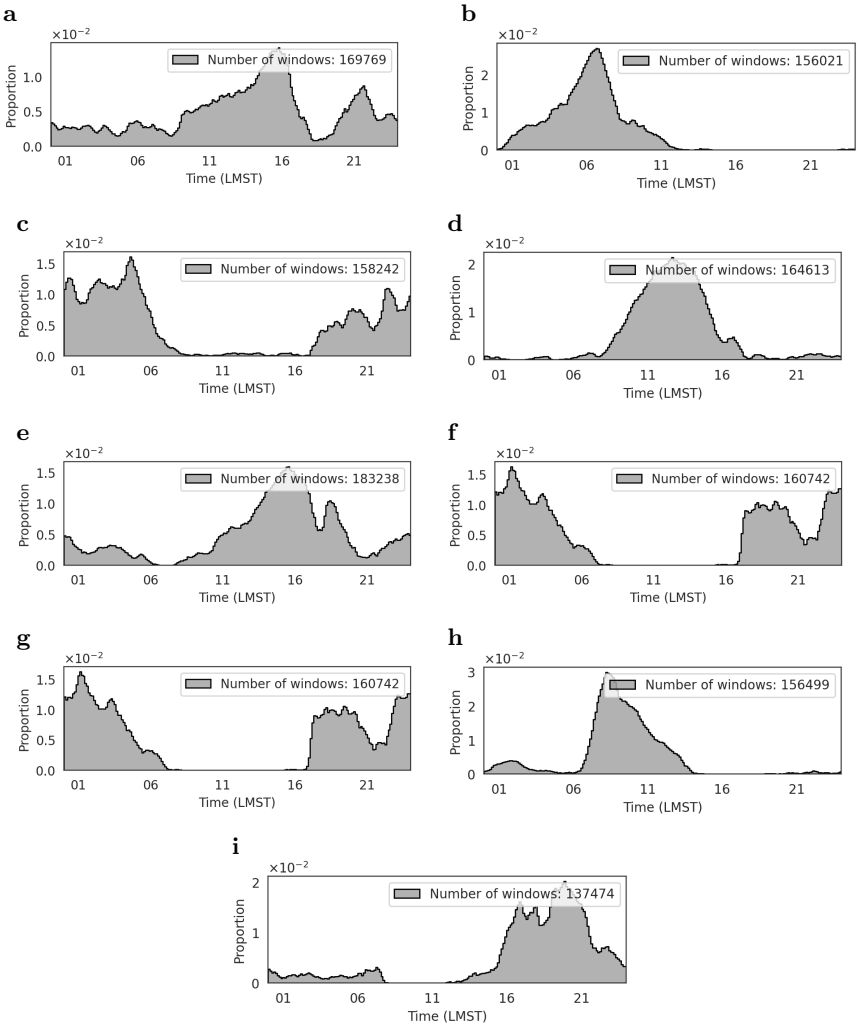

Fig. A7: The occurrence time histogram of all nine identified clusters within the 54.6-minute timescale. The horizontal axis of the histograms represents the local mean solar time (LMST). Clusters 0–9 are shown in Figs. A7a to A7i, respectively.

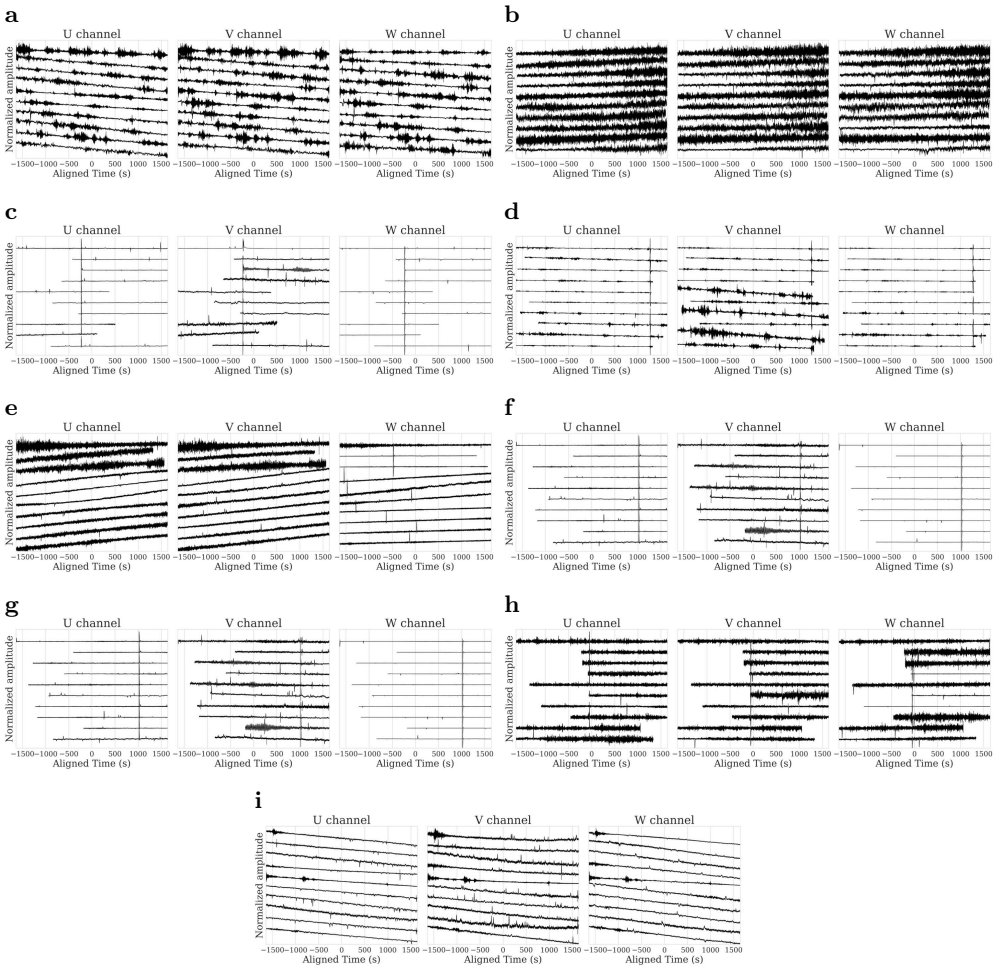

Fig. A8: The aligned waveforms of all nine identified clusters within the 54.6-minute timescale. Clusters 0–9 are shown in Figs. A8a to A8i, respectively.

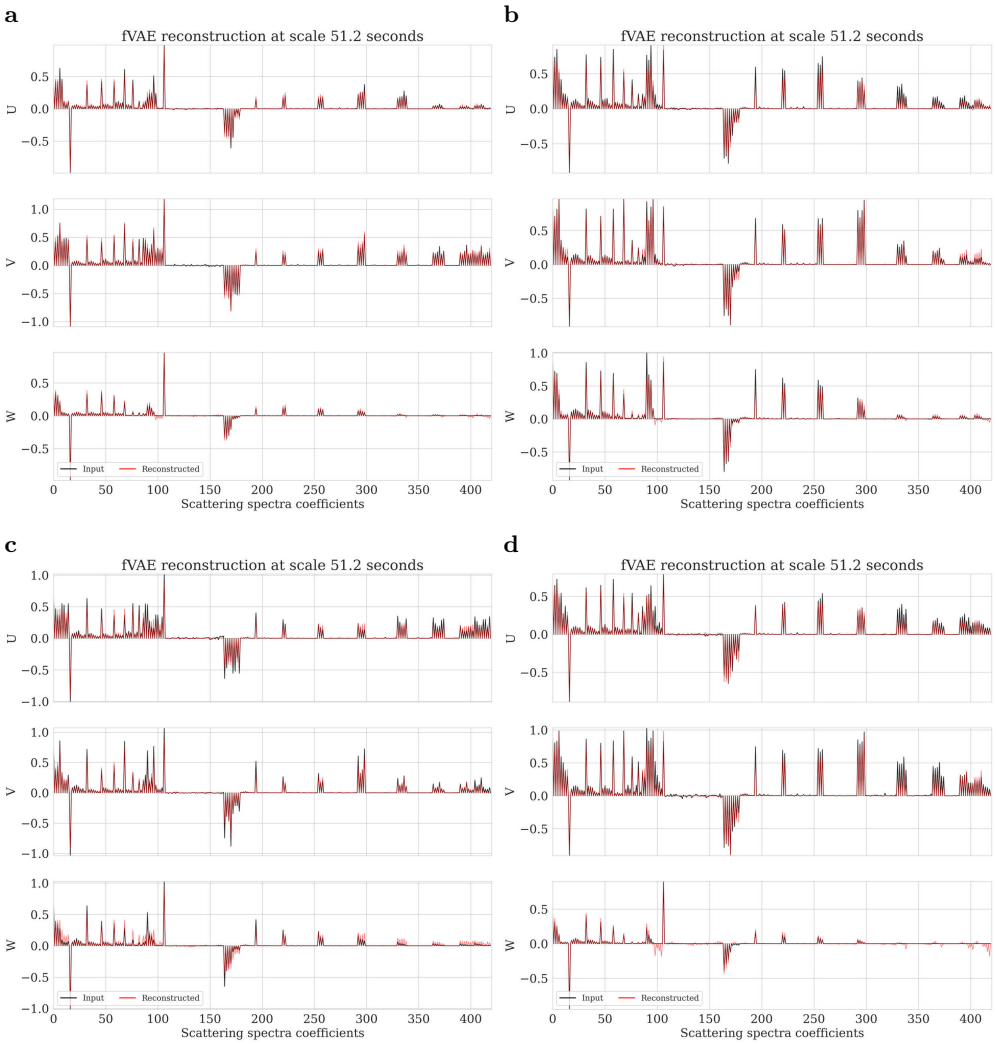

Fig. B9: The input scattering spectra (black) and reconstruction via the fVAE decoder (red) for the U, V, and W components of four random windows from the 51.2-second timescale.

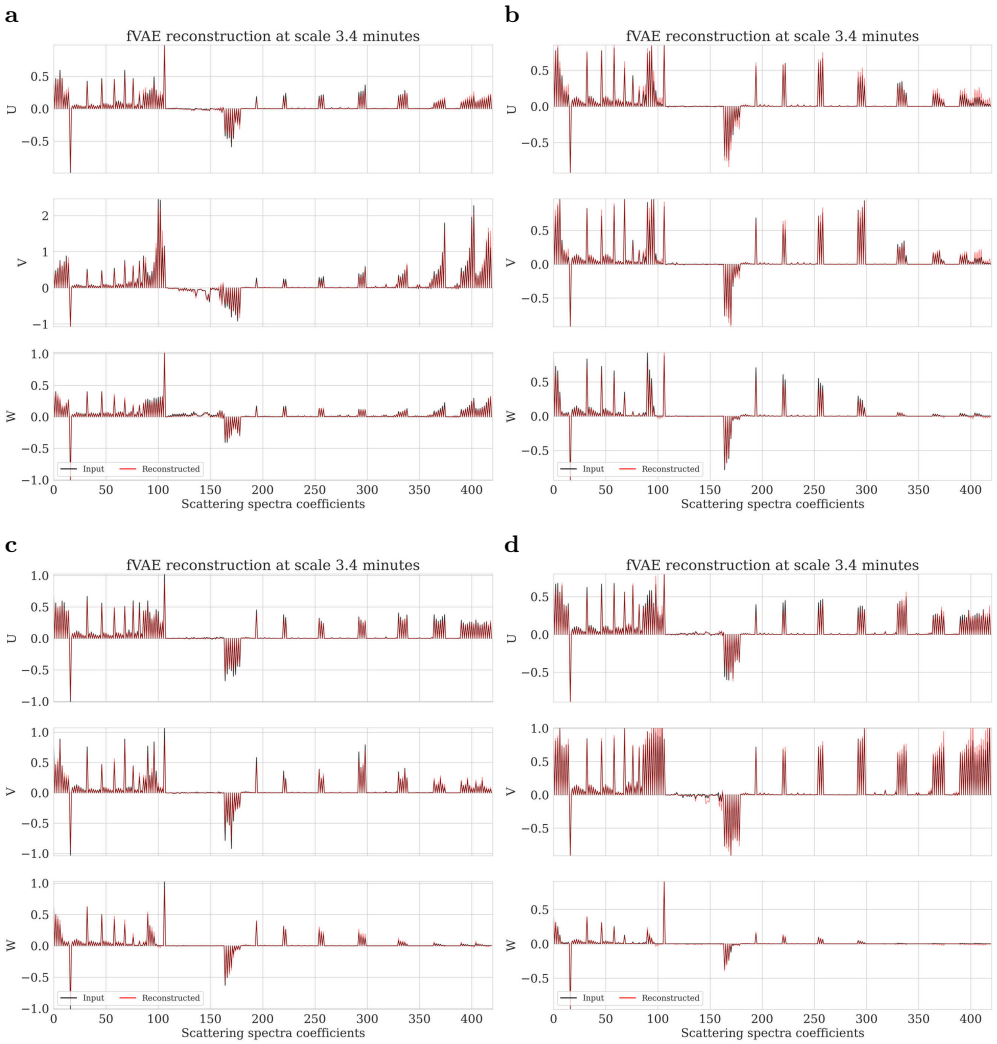

Fig. B10: The input scattering spectra (black) and reconstruction via the fVAE decoder (red) for the U, V, and W components of four random windows from the 3.4-minute timescale.

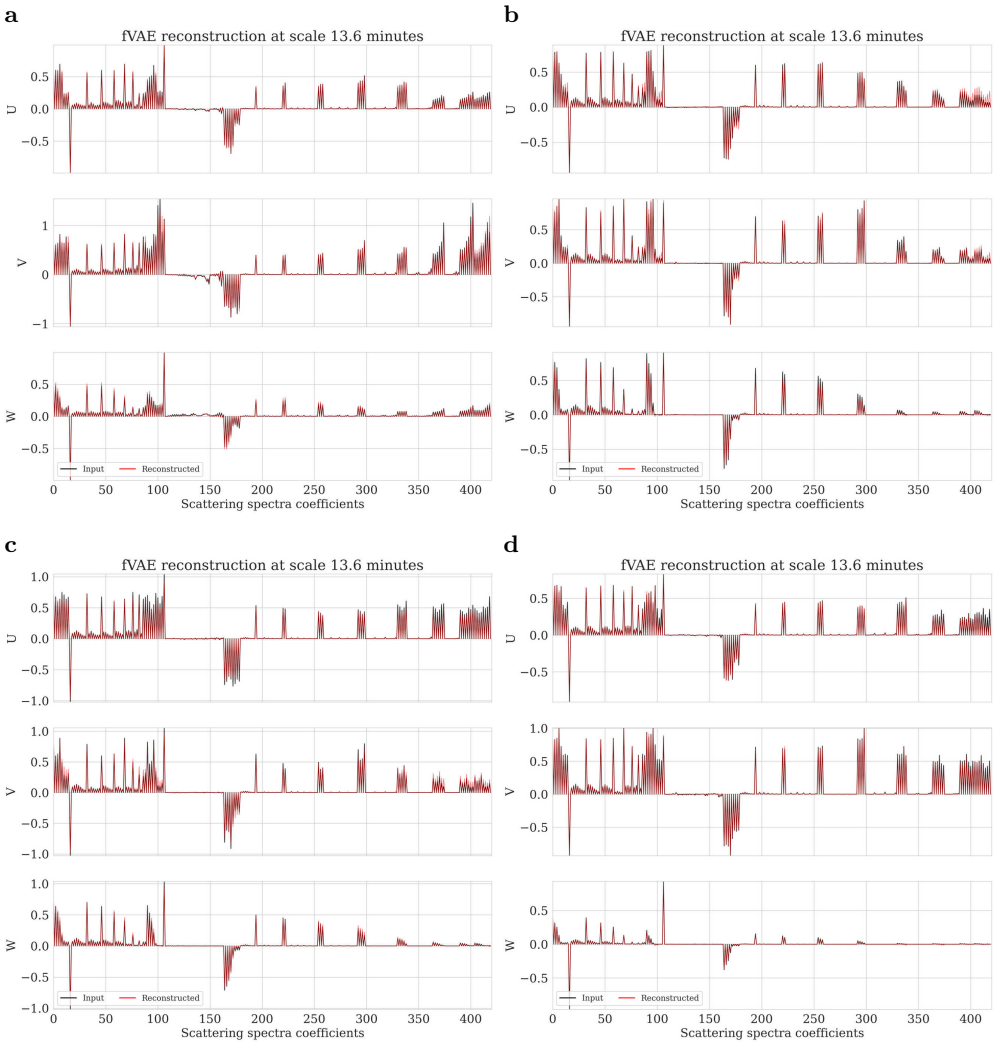

Fig. B11: The input scattering spectra (black) and reconstruction via the fVAE decoder (red) for the U, V, and W components of four random windows from the 13.6-minute timescale.

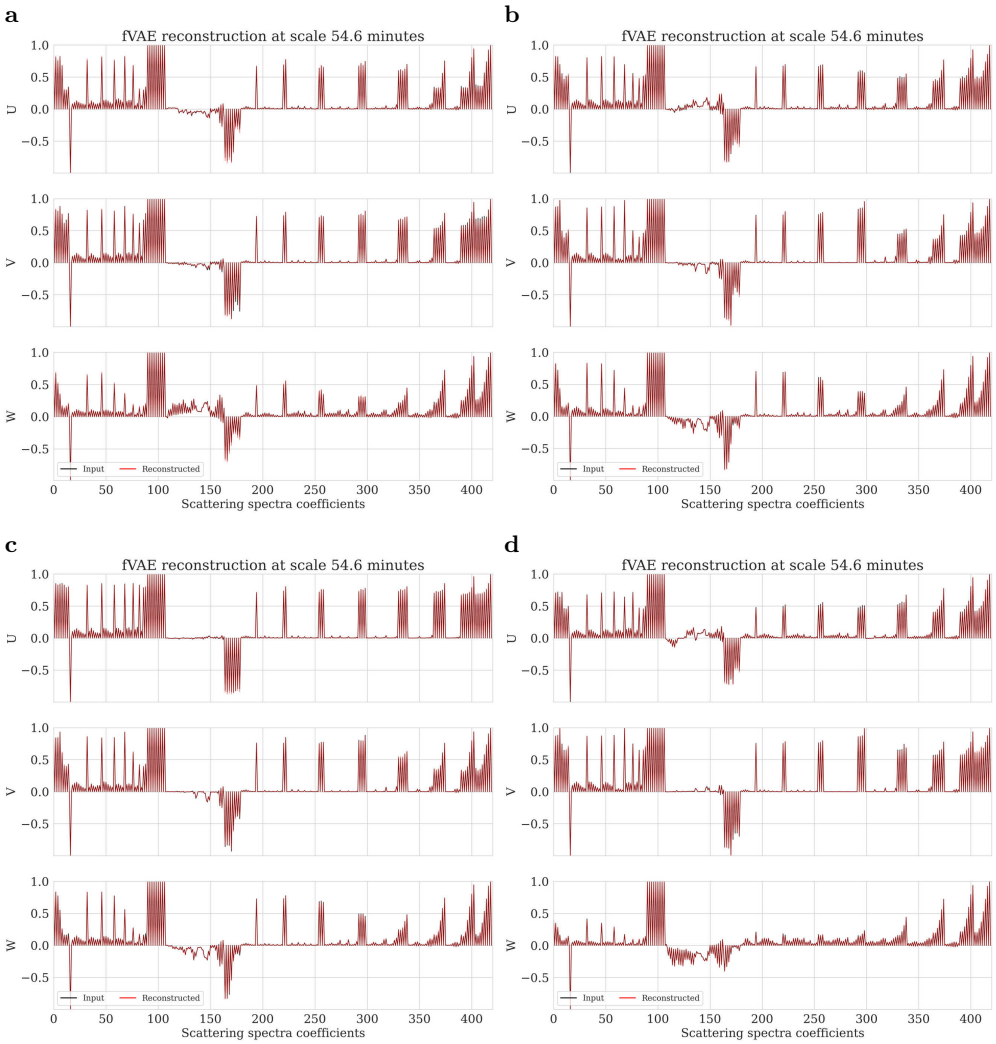

Fig. B12: The input scattering spectra (black) and reconstruction via the fVAE decoder (red) for the U, V, and W components of four random windows from the 54.6-minute timescale.